1-1-2013

# Quantitative Reconstruction and Two-Dimensional, Steady Flow Hydrodynamics of the Plesiosaur Flipper

Mark Cruz DeBlois
deblois@marshall.edu

# QUANTITATIVE RECONSTRUCTION AND TWO-DIMENSIONAL, STEADY FLOW HYDRODYNAMICS OF THE PLESIOSAUR FLIPPER

Thesis submitted to
the Graduate College of
Marshall University

In partial fulfillment of
the requirements for the degree of
Master of Science
in Biological Science

By

Mark Cruz DeBlois

Approved by

Dr. F. Robin O'Keefe, Ph.D., Advisor, Committee Chairperson
Dr. Paul Constantino, Ph.D.
Dr. Suzanne Strait, Ph.D.

Marshall University

May 2013

# ACKNOWLEDGEMENTS

I would like to thank Robin O'Keefe for his tireless mentorship inside the lab and his friendship outside. He has guided me through the threshold of not just the field of paleontology but also functional morphology and biomechanics. Second I would like to thank James Denvir from Marshall University. The parsing script that Jim wrote for this project made it possible to handle and analyze enormous amounts of data. Without his code, this project would not have attained the scope that it has now. I would also like to thank Mark Menor, my dear friend from the University of Hawaii, Manoa. Mark has been my guide as I learned to write code in general and in Matlab specifically. I would have been utterly lost in the world of computer programming without his help. I would like to thank my comrades in arms at Robin's paleo lab: Josh Corrie, Christina Byrd, and Alex Brannick. They have been there to cheer and commiserate with me through the ups and downs of this project. I would like to thank Lyndsay Rankin. She has been my biggest fan and tireless supporter. Lastly I would like to thank my family who has and will always be there behind me to provide support, encouragement, and solace. You all have made this project possible. To all of you, thank you.

This project is dedicated to my family especially Papa and Mama.
I love you all.

# TABLE OF CONTENTS

# LIST OF TABLES

# LIST OF FIGURES

# LIST OF VARIABLES

Re = Reynolds number

$U$ = velocity of flow

$\eta$ = kinematic viscosity of water ($\eta = 1.0 \times 10^{-6}$ $m^2/s$)

$C_L$ = coefficient of lift

$C_D$ = coefficient of drag

$C_P$ = coefficient of pressure

$C_f$ = skin-friction coefficient

$C_{dissipation}$ - the dissipation coefficient

S = hydrofoil surface area

$\rho$ = density of fluid

L = lift

D = drag

$C(\psi)$ = class function

$x$ = x-coordinate

$c$ = chord length

$$\psi = \frac{x}{c}$$

$S(\psi)$ = shape function

$n$ = order of the Bernstein Polynomial ($n = 3$)

$\frac{n!}{r!(n-r)!}$ = binomial coefficient

$A_r$ = CST coefficient to be set using leas-squares fitting ($A_1$ to $A_4$)

$Z(\psi)$ = function of the parameterized hydrofoil

$z_{TE,top}$ = trailing edge tip y-value for the top half (= 0)

$\Delta z_{top} = \frac{z_{TE,top}}{c}$ = thickness of the trailing edge tip of the top half (= 0)

$z_{TE,bottom}$ = trailinge edge tip y-value for the bottom half (= 0)

$\Delta z_{bottom} = \frac{z_{TE,bottom}}{c}$ = thickness of the trailing edge tip of the bottom half (= 0)

$\Phi$ = the streamfunction

$\gamma$ = vortex distribution

$\sigma$ = strength of the source distribution

$x,y$ = x,y-coordinates of a point on the flow field

$s$ = a point along the panel

$r$ = magnitude of the vector between the points $x,y$ and $s$

$\alpha$ = angle of the vector between the points x,y and $s$

$q_\infty$ = freestream velocity

$u_\infty = q_\infty \cos\alpha$, component of $q_\infty$

$v_\infty = q_\infty \sin\alpha$, component of $q_\infty$

$\bar{x} = x\cos\alpha + y\sin\alpha$

$u_{edge}$ = flow velocity at the edge of the boundary layer

$H$ = shape parameter

$H^*$ = kinetic energy shape parameter

$H^{**}$ = the density shape parameter

$\theta$ = boundary layer thickness

$\xi$ = boundary layer coordinate

$M$ = Mach number

$M_{edge}$ = Mach number at the edge of the boundary layer ($M_{edge} = 0$)

$Re_{\theta}$ = Reynolds number multiplied by $\theta$

$\tilde{n}$ = amplitude of the largest Tollmien-Schlichting wave

$\omega$ = aerodynamic frequency parameter (also known as the reduced frequency value)

$f$ = wingbeat frequency

# LIST OF EQUATIONS

# ABSTRACT

Plesiosaurs are a group of extinct marine reptiles that thrived during the Mesozoic Era. They are unique for swimming with two hydrofoil-shaped flippers. Penguins, sea turtles, and cetaceans all have hydrofoil shaped flippers but penguins and sea turtles only use the front pair to produce thrust and cetaceans use their tail flukes. Consequently, the mode of swimming for plesiosaurs has long been debated. However, a quantitative study of the hydrodynamic properties of the flippers, which would constrain inference about their mode of swimming, has not yet been done. The main reason is that the trailing edge of the plesiosaur flipper is made up of soft tissue and does not fossilize. I present in this study a way to quantitatively reconstruct the shape of the functional flipper hydrofoil of the plesiosaurs. Subsequently, I present the first quantitative description of the hydrodynamic properties of plesiosaur flippers.

# INTRODUCTION

Plesiosaurs are a group of extinct secondarily marine tetrapods unique for evolving two pairs of hydrofoil-shaped flippers (Figure 1) (Robinson, 1975, 1977; Massare, 1994; Carpenter et al., 2010). Other animals, like penguins and sea turtles, also have hydrofoil-shaped flippers but these animals have distinctly different forelimb and hind limb morphologies, and rely primarily on the forelimbs for swimming (Massare, 1994; Dodd, 1988; Wyneken, 1997; Davenport et al., 1984). Since there are no extant modern analogs to plesiosaurs, their manner of locomotion has long been debated. Prior studies on plesiosaur flipper anatomy suggest that they likely propelled the animal by producing lift (De La Beche and Conybeare, 1821; Robinson, 1975; Brown, 1981; Taylor, 1981; Frey and Reiss, 1982; Tarsitano and Reiss, 1982; Massare, 1994; Carpenter et al., 2010), raising the possibility that plesiosaurs 'flew' through the water. However, others assert that the flippers propelled the animal by pushing against the fluid acting as rowing paddles instead of hydrofoils (Watson, 1924). Some have proposed a combination of the two with the forelimbs producing lift while the hind limbs push against the water (Tarlo, 1957). Still others have proposed a swimming motion similar to otariids (sea lions) (Godfrey, 1984). Despite the keen interest in plesiosaur locomotion, no one has yet directly studied the hydrodynamics of plesiosaur flippers. The widely held contemporary view (Storrs, 1993; O'Keefe, 2001b; Carpenter et al., 2010) is that plesiosaur flippers produced lift, but because no one has yet quantified the hydrodynamic properties of the flippers, the amount of lift (and drag) produced by the flipper is unknown. The present study is the first to quantitatively investigate the hydrodynamics of plesiosaur flippers from a variety of different plesiosaur taxa. Moreover since locomotion plays a vital role in an animal's biology, understanding the hydrodynamics of the flippers will provide insight into and constrain inference about plesiosaur biology.

# CHAPTER 1: BACKGROUND

## PLESIOSAURIA

### Distribution and Phylogeny

The Infra-order Plesiosauria, de Blainville 1835 (literally "near-lizards") comprises a monophyletic clade of extinct fully aquatic Mesozoic marine reptiles (O'Keefe, 2001a; Ketchum and Benson, 2010). They first appeared in the Rhaetian during the late Triassic Period approximately 200 million years ago (Mya) (Storrs, 1993, 1997; Rieppel, 1997) and thrived until the mass extinction event at the Cretaceous – Tertiary (K-T) boundary approximately 65 Mya (Storrs, 1997). During their 135 million year reign, plesiosaurs established a worldwide distribution extending from North America (Nicholls and Russell, 1990) to Europe (Andrews, 1913), north to Greenland (von Huene, 1935 cited in Smith, 2007) and south to Australia and New Zealand (Kear, 2003; Kear et al., 2006; Cruickshank and Fordyce, 2003). Plesiosaurs are the most derived and successful members of the Order Sauropterygia, Owen 1860 (see Figure 2; Rieppel, 2000; O'Keefe, 2001a; Storrs, 1997; Druckenmiller and Russell, 2008; Ketchum and Benson, 2010). Plesiosauria is most closely related to Pistosauridae and other plesiosaur-like nothosaurs (nothosaur-grade taxa), altogether comprising the subclade Pistosauroidea (Rieppel, 2000; O'Keefe, 2001a; Druckenmiller and Russell, 2008). In turn, Pistosauroidea together with the subclades Nothosauria and Pachypleurosauroidea comprise the clade Eosauropterygia. Finally, Eosauropterygia and Placodontia comprise Sauropterygia (see Figure 2; Rieppel, 2000; O'Keefe, 2001a; Druckenmiller and Russell, 2008). Sauropterygia originated in the Upper Permian and likely descended from primitive terrestrial diapsid reptiles (Carroll, 1981; Storrs, 1993; Neenan et al., 2013).

Plesiosauria is divided into two monophyletic superfamilies: Plesiosauroidea and Pliosauroidea (O'Keefe, 2001a; Ketchum and Benson, 2010; Benson et al., 2012). Plesiosauroidea consists of five families: Plesiosauridae, Elasmosauridae, Cryptoclididae, Leptocleididae, and Polycotylidae (see Figure 3; Ketchum and Benson, 2010). Pliosauroidea consists of two major families: Rhomaleosauridae and Pliosauridae (see Figure 3; O'Keefe, 2001a; Ketchum and Benson, 2010; Benson et al., 2012). Plesiosauridea are basal plesiosauroids whereas Elasmosauridae, and Polycotylidae are derived crown group plesiosauroids. Likewise, Rhomaleosauridae are basal pliosauroids whereas Pliosauridae are derived crown group pliosauroids (O'Keefe 2001a; Ketchum and Benson, 2010; Benson et al., 2012). However, recent work by Benson and colleagues (2012) suggest that Pliosauroidea constitutes a paraphyletic group. In this scheme, Pliosauridae forms a monophyletic clade with Plesiosauroidea (Neoplesiosauria) with Rhomaleosauridae as the immediate outgroup (Benson et al., 2012). The phylogenetic position of Polycotylidae has fluctuated between the two superfamilies owing to its similarity to both (Figure 1) with some authors placing it within Pliosauroidea (Andrews, 1910, 1913; Welles, 1952; Brown, 1981; Brown and Cruickshank, 1994) while others authors place it in Plesiosauroidea (O'Keefe, 2001a, 2002; Ketchum and Benson, 2010 and references therein). However since the most recent phylogenetic analysis of Plesiosauria by Ketchum and Benson (2010) places Polycotylidae firmly in Plesiosauroidea, Polycotylidae will be treated as belonging to Plesiosauroidea for the present study.

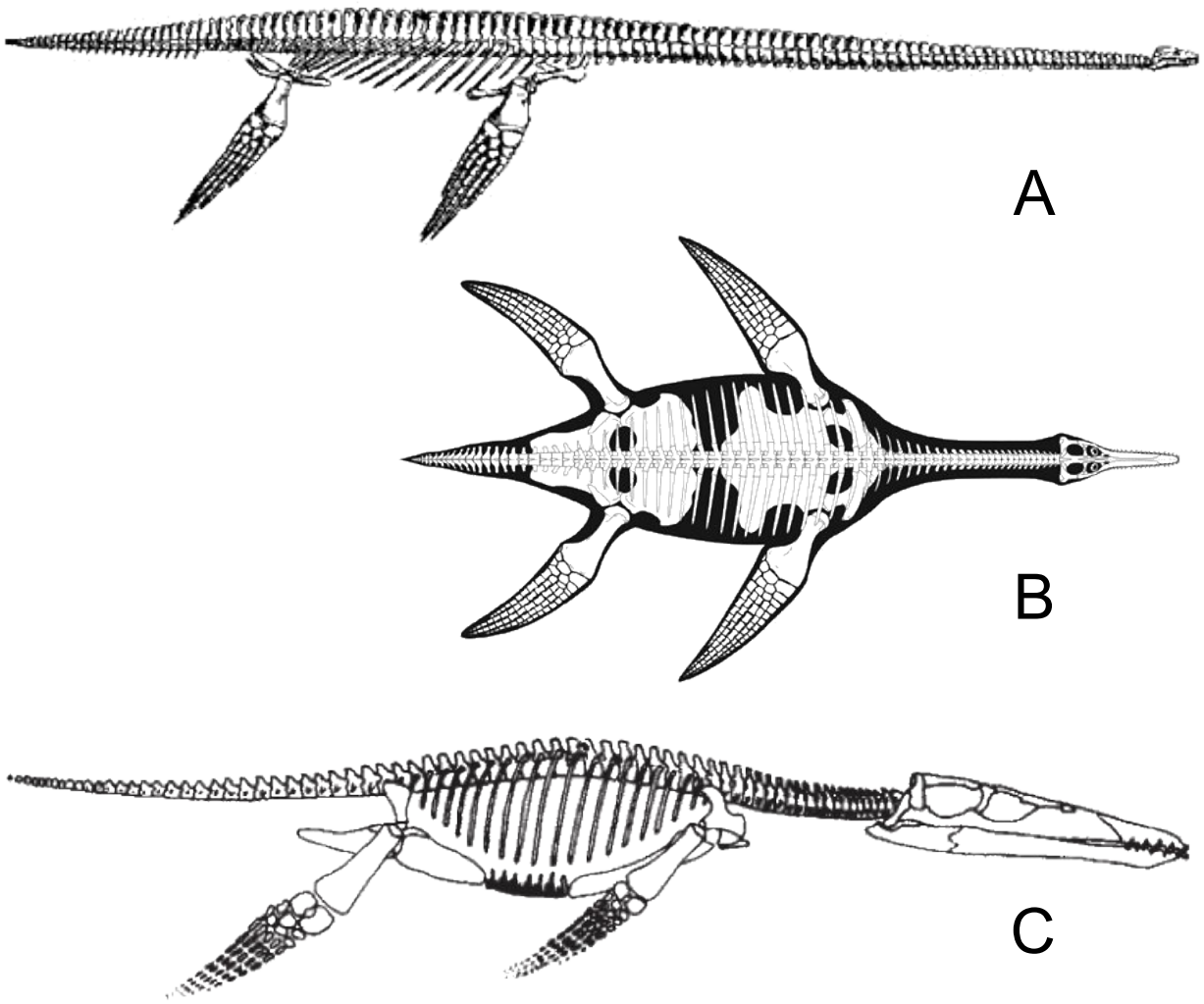


Figure 1. Representative plesiosauromorph and pliosauromorphs. Not to scale. (**A**) *Hydrotherosaurus*, a plesiosauromorph belonging to Elasmosauridae in the superfamily Plesiosauroidea. Lateral view. From O'Keefe, 2002. (**B**) *Polycotylus*, a pliosauromorph belonging to Polycotylidae in the superfamily Plesiosauroidea. Top view. Adapted from O'Keefe, 2009. (**C**) *Liopleurodon*, a pliosauromorph belonging to Pliosauridae in the superfamily Pliosauroidea. Lateral view. From O'Keefe, 2002.

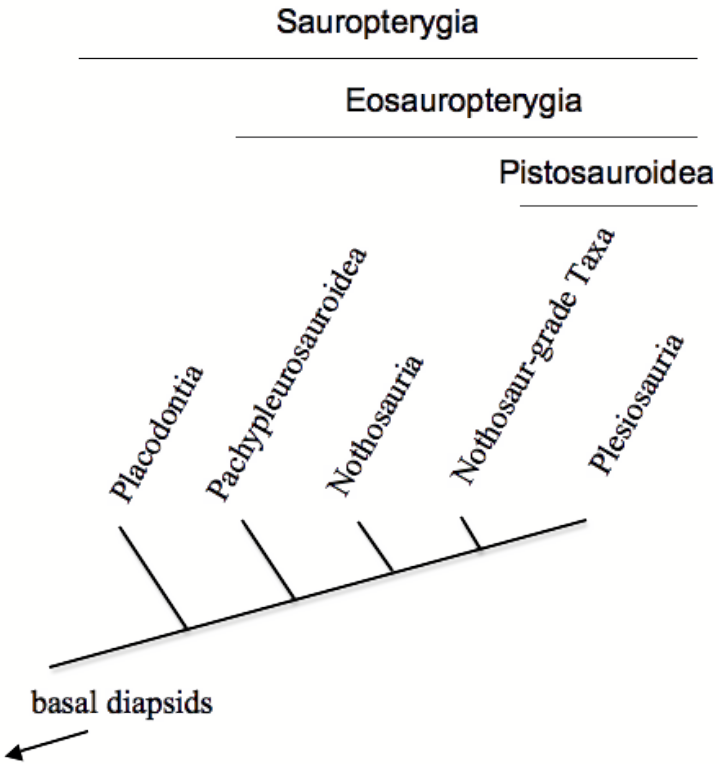


Figure 2. Cladogram showing the interrelationships within the Order Sauropterygia based on work by Rieppel (2000).

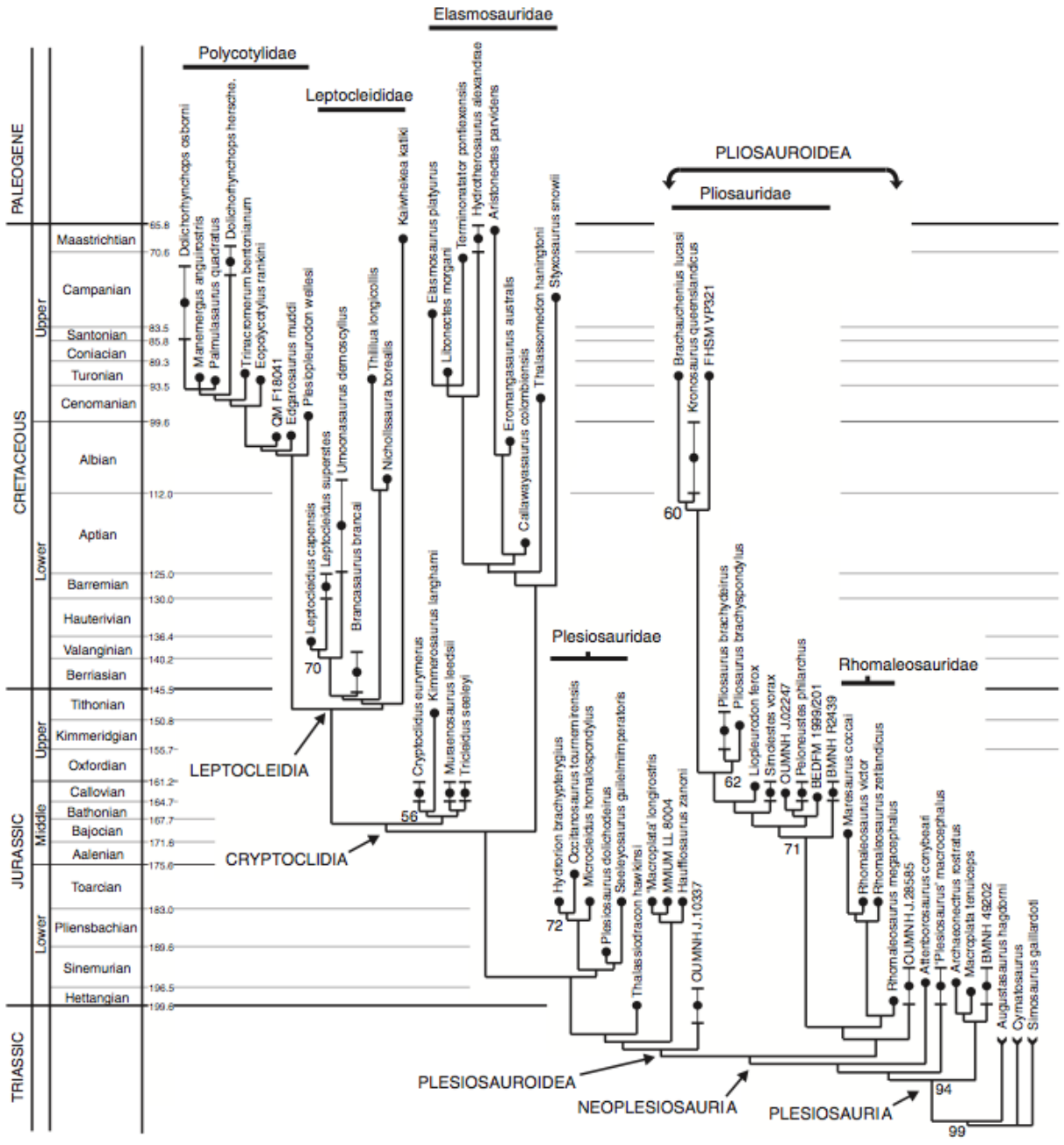


Figure 3. Phylogenetic tree from Ketchum and Benson (2010) showing the relationships of taxa within Plesiosauria as well as their respective temporal distributions. Note the positions of Elasmosauridae and Polycotylidae within Plesiosauroidea and Pliosauridae within Pliosauroidea.

**Morphotypes**

Plesiosauria has traditionally been divided into two groups based on body plans (morphotypes) (for a list of defining characters see Table 1) (Brown, 1981; O'Keefe, 2001b, 2002; Ketchum and Benson, 2010). Those with relatively small heads and long necks (labeled as plesiosauromorphs) were traditionally grouped together and considered taxonomically distinct from those with relatively large heads and short necks (labeled as pliosauromorphs, see Figure 1) (Andrews, 1910, 1913; Welles, 1952; Brown, 1981; Brown and Cruickshank, 1994). This dichotomy was challenged as early as 1907 by Williston and recent work has shown that the pliosauromorph body plan likely evolved independently in several different lineages (Carpenter, 1997; O'Keefe, 2001a, 2002; Ketchum and Benson, 2010; Benson et al., 2012). The plesiosauromorph – pliosauromorph dichotomy, therefore, does not correspond to any phylogenetic division within Plesiosauria and, instead, represents a polyphyletic assemblage of taxa. Pliosauridae, Rhomaleosauridae, and Polycotylidae all have the pliosauromorph body plans but Polycotylidae is more closely related to Elasmosauridae, a plesiosauromorph, than to either Pliosauridae or Rhomaleosauridae (see Figure 3) (O'Keefe 2001a, 2002; Ketchum and Benson, 2010). Furthermore, even though Pliosauridae and Rhomaleosauridae are closely related, their lineages appear to have diverged before the pliosauromorph body plan was crystallized (O'Keefe, 2001a, 2002). Indeed, work by O'Keefe (2002) suggests that the plesiosauromorph and pliosauromorph distinction is *not* a dichotomy but instead represents a spectrum of morphotypes with Elasmosauridae and Pliosauridae at opposite extremes.

Although invalid phylogenetically due to polyphyly, the plesiosauromorph and pliosauromorph groupings represent instances of convergent evolution that provide provocative insight into the ecology and paleobiology of plesiosaurs. Plesiosauromorphs have been

Table 1: Defining characters of plesiosauromorph and pliosauromorph body types. Adapted from O'Keefe (2002), *O'Keefe (2001b), and **Massare (1988).

| **Body part** | **Plesiosauromorph** | **Pliosauromorph** |
|---|---|---|
| Skull | Relatively small | Relatively large |
| Position of orbits** | Upwards and forward | Lateral |
| Number of cervical vertebrae | ≥ 28-32 | < 28 |
| Dimensions of cervical vertebrae | As long as or longer than wide | Shorter than wide |
| Fore- and hind-limb proportions | Forelimb > hind limb | Forelimb < hind limb |
| Limb aspect ratio (in general)* | High | Low |
| Scapula | Relatively long | Relatively short |
| Ischium | Relatively short | Relatively long |

hypothesized to be cruising predators while pliosauromorphs have been hypothesized to be active pursuit predators based on body proportions (Table 1) (Robinson, 1975; Massare, 1988; O'Keefe, 2002) combined with estimates of swimming speed (Massare, 1988; Motani, 2002) and swimming capability (O'Keefe, 2001b). The small head and teeth of plesiosauromorphs would have limited them to smaller more abundant prey whereas the large head and teeth of pliosauromorphs would have been better suited for catching and consuming larger less abundant prey (Massare, 1988). Furthermore, the upward and forward facing orbits of plesiosauromorphs would have facilitated prey ambush from below whereas the lateral (as opposed to upward) facing orbits of pliosauromorphs would have facilitated tracking prey at the same level as the animal such as during a pursuit (Massare, 1988). Plesiosauromorphs, with their heads so far ahead of the main body, would have been able to sneak up on unsuspecting prey unlike the short-necked pliosauromorphs (Massare, 1988). However, plesiosauromorphs would not have attained the same speeds as pliosauromorphs because their necks would have caused them to be less streamlined than the more fusiform-shaped pliosauromorphs (Massare, 1988).

Plesiosauromorphs have high aspect ratio flippers, which coincide with aerodynamic trends for

efficiency, while pliosauromorphs have low aspect ratio flippers, which coincide with aerodynamic trends for speed and maneuverability (O'Keefe, 2001b). Altogether, plesiosauromorphs *appear* to be slow but efficient cruising predators that relied on stealth to catch small, abundant prey. In contrast, pliosauromorphs *appear* to be maneuverable but inefficient high-speed burst predators that would have had to pursue and catch large, less abundant prey. However, the hypothesized ecomorphology of plesiosauromorphs and pliosauromorphs remain untested and speculative. The predatory behaviors of long extinct animals are impossible to test but the hydrodynamic properties of their flippers can be assessed, which would constrain inference by providing strong functional evidence in support of (or against) the hypothesized ecomorphology of plesiosauromorphs and pliosauromorphs.

## PROPERTIES OF HYDROFOILS

### Sources of Lift and Drag

*Lift*. Hydrofoils are curved surfaces with a blunt leading edge and a pointed trailing edge (Figure 4). Fluid flowing from the leading edge to the trailing edge produces a force (lift) perpendicular to the flow stream and pointed in the direction of positive curvature (see Figure 4) (Vogel, 1994; Abbott and von Doenhoff, 1959). Fluid flows faster along the positively curved surface (convex side) and slower along the negatively curved surface (concave side). Consequently, lower pressure is produced along the positively curved surface and higher pressure is produced along the negatively curved surface according to Bernoulli's principle. This difference in pressure produces net lift (Vogel, 1994; Abbott and von Doenhoff, 1959).

Airplane wings and other airfoils (man-made or biological) have dorsally oriented (positive) curvature and, conversely, ventrally oriented (negative) curvature. This is to combat

gravity and keep the plane or animal aloft by producing upward lift. However, hydrofoils need not have to oppose gravity underwater. The greater density of water compared to air enables the manipulation of buoyancy to oppose gravity and thereby control one's location in the water column. Furthermore, buoyancy is independent of the orientation of the submerged body and is always directed upwards, away from gravity. This frees up hydrofoils from having to constantly counteract gravity and, instead, be used primarily for thrust production and body-orientation control. This means that hydrofoils need not have dorsally oriented (positive) curvature.

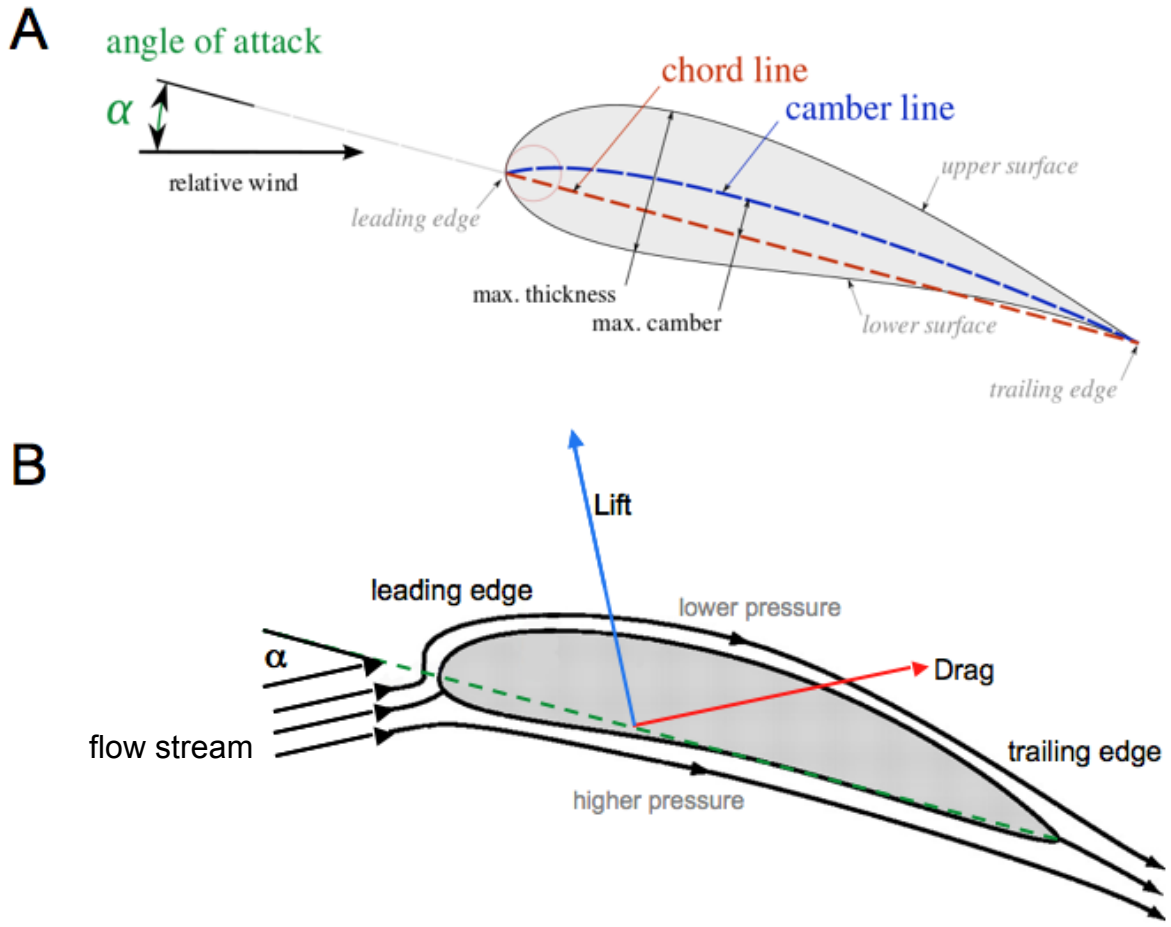


Figure 4. Diagram of a hydrofoil cross-section (**A**) and how it interacts with the flow stream to produce the aerodynamic forces of lift and drag (**B**). Modified from Sane, 2003.

*Drag.* The movement of fluid along the hydrofoil produces another force, that of drag. Drag is analogous to friction in that it is directed in the direction of the flow and away from the direction of movement (Vogel, 1994; Abbott and von Doenhoff, 1959). There are three sources of drag: skin friction, pressure drag, and induced drag (Vogel, 1994). Skin friction results from the shearing force created as the hydrofoil moves through the fluid (Vogel, 1994). Skin friction is dependent on the viscosity of the fluid and the surface area of the hydrofoil: the higher the viscosity, the more the fluid resists shearing and the greater the drag; the greater the surface area, the greater the space over which shearing occurs and the greater the drag (Vogel, 1994).

The second source of drag is pressure drag and it occurs as a result of flow separation and the imbalance between the pressures at the leading edge and the trailing edge (see Figure 4) (Vogel, 1994). In effect, it is equivalent to the energy lost as the fluid is accelerated over the hydrofoil (Vogel, 1994). Fluid coming in contact with the leading edge of the hydrofoil (Figure 4) accelerates as it goes over the blunt leading edge and up along the hydrofoil, requiring energy. This energy is lost as the fluid flows past the hydrofoil by being dissipated in the wake as the streamlines separate (Vogel, 1994). However, this energy loss is mitigated and part of it is even recovered in streamlined hydrofoils, those with long tapering trailing edges in the direction of the flow (Vogel, 1994). In these hydrofoils, the fluid decelerates as it flows down the trailing edge and little to no flow separation occurs (Vogel, 1994). In addition, the wedge-like closure of the fluid behind the hydrofoil creates a forward directed pressure that *nearly* counterbalances the backward directed dynamic pressure in the leading edge (Vogel, 1994). Thus even in streamlined hydrofoils, some energy is still lost. Skin friction and pressure drag together make up what is known as profile drag (Vogel, 1994).

Profile drag results from 2-dimensional forces acting on wing cross-sections whereas the third source of drag, induced drag, results from the 3-dimensional shape of the wing. Because wings have a finite span, fluid can flow from one surface to the other over the wingtip resulting in a vortex in the direction of low pressure (Abbott and von Doenhoff, 1959; Vogel, 1994). Energy is lost in the formation of this vortex (Vogel, 1994). Moreover, this vortex acts on the oncoming flow streams (those directed from leading edge to trailing edge) resulting in net flow that is tilted in the direction of vortex flow (Abbott and von Doenhoff, 1959). This changes the angle of attack immediately around the wing (Figure 4) resulting in drag that is larger than would be expected for the same angle of attack under 2-D flow conditions (Abbott and von Doenhoff, 1959).

Analysis of hydrofoils in the present study is limited to 2-dimensional, steady flow around the cross-sectional shape of plesiosaur hydrofoils thus the value for drag will solely reflect profile drag with no contribution from induced drag.

**Flow Effects on Lift and Drag**

*Reynolds number (Re) and Fluid Properties*. Lift and drag depend on the interaction between the shape of the hydrofoil and the physical properties of the fluid medium, namely the density, velocity, and Reynolds number (Re) (Vogel, 1994; Abbott and von Doenhoff, 1959). Reynolds number is a ratio of the inertial forces over viscous forces that characterize the fluid (Vogel, 1994). Inertial forces are attributable to the momentum of a particle in the fluid whereas viscous forces are attributable to the resistance of the fluid to pull apart and separate (Vogel, 1994). According to Vogel (1994), inertial forces reflect the "individuality" of fluid particles whereas viscous forces reflect their "groupiness". Re is give by:

$$Re = cU/\eta \quad (1)$$

where $c$ is the chord length of the hydrofoil, $U$ is the velocity of the flow, and $\eta$ is the kinematic viscosity of water ($\eta = 1.0x10^{-6}$ $m^2/s$). At low Reynolds numbers ($Re < 500,000$), viscous forces dominate and the flow is laminar. At high Reynolds numbers ($Re > 1,000,000$), inertial forces dominate and the flow is turbulent (Vogel, 1994). Inertial and viscous forces are still present at low and high Re, respectively, but the effect of one is dwarfed by the effect of other (Vogel, 1994). This means, for example, that drag at low Re is mainly due to skin friction while at high Re, drag is mainly due to pressure drag (Vogel, 1994; Abbott and von Doenhoff, 1959). The transition from laminar to turbulent flow for streamlined shapes occurs at Reynolds numbers between 500,000 and 1,000,000 ($10^5 < Re < 10^6$) (Vogel, 1994). The effects of Re on lift and drag for a given shape are complex and vary at each value of Re. This relationship is encapsulated in the coefficient of lift ($C_L$) and the coefficient of drag ($C_D$), which vary as a function of Re (Vogel, 1994). Therefore, for a given hydrofoil surface area (S), fluid density ($\rho$), and velocity (U), the lift (L) and drag (D) produced by an object is expressed as (Abbott and von Doenhoff, 1959; Vogel, 1994):

$$L = 1/2\rho SU^2C_L \quad (2a)$$

$$D = 1/2\rho SU^2C_D \quad (2b)$$

*Angle of Attack.* The angle of attack ($\alpha$) is the angle made by the orientation of the hydrofoil (specifically the chord line, see Figure 4) with respect to the direction of oncoming flow localized around hydrofoil (Figure 4) (Vogel, 1994). The direction of flow over the entire animal may be quite different from the direction of flow with respect to the hydrofoil, especially

during the dynamic movements associated with biological locomotion. Indeed, induced drag (discussed above) reduces the amount of lift produced by altering the local flow around the hydrofoil, in effect reducing the angle of attack (Abbott and von Doenhoff, 1959). As the angle of attack increases, so does lift and the two are nearly linearly related. Lift reaches a maximum value ($C_{Lmax}$) at the critical angle of attack (also known as the stall angle, so named because the value for lift plummets past this angle of attack) (Vogel, 1994; Abbott and von Doenhoff, 1959). Lift is reduced because flow on the surface of positive curvature separates from the surface of the hydrofoil near the leading edge (Vogel, 1994; Webb, 1975; Fish and Battle, 1995). Drag also tends to increase as the angle of attack ($\alpha$) increases, but unlike lift, the plot of drag as a function of $\alpha$ resembles a parabola with a minimum at low values of lift (Abbott and von Doenhoff, 1959). Drag continues to increase past the stall angle when the amount of lift produced by the hydrofoil is negligible compared to drag (Vogel, 1994).

**Shape Effects on Lift and Drag**

*Chord, Camber, and Thickness.* The cross-sectional length of a wing is defined as the cord. It is the length from the outermost edge of the leading edge to the very tip of the trailing edge (Figure 4). The mean line is the average curvature of the top and bottom surfaces of the hydrofoil and would be indistinguishable with the chord for symmetric hydrofoils (Figure 4).

Camber is a measure of the curvature of the hydrofoil defined as the difference between the mean line and the chord (Figure 4) in proportion to the chord. The asymmetry between the two surfaces facilitates the formation of a pressure difference such that a cambered hydrofoil produces lift even at an angle of attack of zero, when symmetrical hydrofoils would not (Abbott and von Doenhoff, 1959). Increasing the degree of camber pushes the angle that produces zero

lift past zero to negative angles (Abbott and von Doenhoff, 1959). Increasing camber also raises the value of the maximum lift coefficient ($C_{Lmax}$) although the most pronounced increases occur when the camber is small to moderate (Abbott and von Doenhoff, 1959). Increasing camber tends to reduce the value of the minimum drag coefficient ($C_{Dmin}$) although the change is very small (Abbott and von Doenhoff, 1959). Raising $C_{Lmax}$ reduces the minimum velocity necessary to produce enough lift to counterbalance drag and prevent stall (stall speed). Thus hydrofoils with greater camber are effective at slower velocities, which would enable greater maneuverability. The chordwise position of maximum camber affects the severity of the loss of lift past the critical angle of attack: hydrofoils with camber located closer to the leading edge tends to lose lift sharply past the stall angle whereas those with camber further back tends to lose lift more gradually (Abbott and von Doenhoff, 1959).

As with camber, the thickness of the hydrofoil (in proportion to the chord; see Figure 4) affects $C_{Lmax}$ and $C_{Dmin}$ (Abbott and von Doenhoff, 1959). In general, increasing thickness also increases drag (Vogel, 1994). Wind tunnel experiments have shown that increasing the thickness from 6% to 21% of the chord increases $C_{Dmin}$ (Abbott and von Doenhoff, 1959). Interestingly, $C_{Lmax}$ increases quickly as thickness increases from 6% to 12% of the chord then gradually decreases after that (Abbott and von Doenhoff, 1959). Adding camber to the hydrofoil lowers the thickness that produces the highest value for $C_{Lmax}$ (Abbott and von Doenhoff, 1959).

*Aspect Ratio.* Aspect ratio is a measure of the broadness or narrowness of the planform shape of the wing (Vogel, 1994). It is given by the ratio of the tip-to-tip length of the wing (its span) to wing area ($span^2$/wing area), which is equivalent to the ratio of the span to the chord length (Vogel, 1994; O'Keefe, 2001b). The higher the aspect ratio, the narrower the wing becomes. This reduces the effect of induced drag (see above) on the wing resulting in higher

values for $C_L$ and lower values for $C_D$ (Vogel, 1994; Abbott and von Doenhoff, 1959). Conversely the lower the aspect ratio, the broader the wing becomes and the greater the effect of induced drag (Vogel, 1994; Abbott and von Doenhoff, 1959). However in place of less efficiency, low AR (broad) wings are more maneuverable by enabling slower 'flight' speed and tighter turning radii (O'Keefe, 2001b). There are ways to reduce the cost of having low AR wings; wings that taper distally or are swept back reduce the magnitude of induced drag (Fish, 2004; Vogel, 1994).

**Study Parameters**

Lift and drag depend on the complex interaction of the physical properties of the fluid, the angle of attack, and shape of the hydrofoil (its camber, chord length, and thickness) (see Figure 4) (Abbott and von Doenhoff, 1959). Due to the complexity of these interactions, mathematical approximations must be combined with empirical measurements from flow tanks in order to provide an accurate assessment of the performance of a given hydrofoil (Abbott and von Doenhoff, 1959). Purely mathematical approximations alone, based upon ideal physical assumptions provide a poor estimate of real-world performance and must be combined with empirical data from flow tanks (Abbott and von Doenhoff, 1959).

For this study, lift and drag will be approximated using XFoil, a widely used airfoil design and simulation program that models streamlines using a combination of viscid and inviscid vortex panelling (Drela, 1989; Drela and Giles, 1987; XFoil program last updated on November 30, 2001). Fluid density, velocity, and Re will be kept constant. Motani (2002) estimated the Re value for plesiosaurs (whole animal) to be between 100,000 and 10,000,000 ($10^5$ to $10^7$). For comparison, dolphins and other odontocete cetaceans as well as seals (phocids)

have a Re value between 1,000,000 and 10,000,000 ($10^6$ to $10^7$) (Fish, 1993, 1998, 2004; Fish et al., 1988). For the present study, Re was set to 10,000,000 (unless otherwise stated) as a simplification in order to avoid the transition between laminar to turbulent flow, which occurs between 500,000 and 1,000,000 as well as reduce the effect of parasitic drag which is predominant at Re < 500,000 (Vogel, 1994). Since lift propels the hydrofoil and drag opposes this motion, the ratio of lift-to-drag is used as an index of hydrofoil efficiency. This value is determined by taking the ratio of the respective coefficients, $C_L$ / $C_D$. Since the degree of camber increases the maximum value of the coefficient of lift ($C_{Lmax}$) and enables slower flight speeds, it will be used as a measure of maneuverability.

## BIOLOGICAL HYDROFOILS

### Extant Hydrofoil-Bearing Tetrapods

Among reptiles, cheloniids (sea turtles), ichthyosaurs (extinct fish-shaped marine reptiles that coexisted with plesiosaurs), and plesiosaurs have hydrofoil shaped (wing-like) flippers (Davenport et al., 1984; Fish, 2004; Massare 1994; Motani 1995; O'Keefe 2001b; O'Keefe and Carrano, 2005). Of these only sea turtles have extant representatives. Turtles have hydrofoil shaped fore flippers that are used to propel and maneuver the animal (Davenport et al., 1984). The hind flippers are used primarily for steering and act as rudders (Dodd, 1988; Wyneken, 1997; Fish, 2004; Massare 1994). Among mammals, cetaceans (whales, dolphins, and porpoises) and pinnipeds (seals and sea lions) have hydrofoil shaped appendages. Cetaceans have a flexible fluke (Fish et al., 2006) that is primarily used to produce thrust (Woodward et al. 2006), a single pair of fore flippers, and a dorsal fin that provides stability (Fish, 2004). Pinnipeds have hydrofoils shaped fore flippers that provide the primary source of thrust for

otariids (sea lions), although the motion of the stroke is a combination of lift-based followed by drag-based propulsion (Feldkamp, 2009). Among birds, spheniscids (penguins) and the extinct plotopterids are the most derived for underwater flight, having given up the use of their wings for aerial flight in favor of underwater flight (Habib, 2010; Lovvorn, 2001; Lovvorn and Liggins, 2002). Semi-aquatic birds like alcids (auks), pelecanoidids (diving-petrels), and cinclids (dippers) use their wings as hydrofoils underwater while retaining the use of their wings for aerial flight (Habib, 2010).

**Anatomical Composition**

Hydrofoil shaped appendages have convergently evolved in several fully aquatic, secondarily marine tetrapods. They are either modifications of the legs and feet (usually the forelegs) or cartilaginous extensions of the spine and tail as in cetacean dorsal fins and flukes. Flippers derived from limbs have been modified to assume a hydrofoil shape. The digits of the feet are no longer separated and the bones are more robustly constructed to accommodate the greater force demands of underwater locomotion (Fish, 2004; Habib, 2010; Wynecken, 2001). In penguins, the bones are more compact and flattened compared to other birds (Bannasch, 1994). Interestingly, the wing bones of semi-aquatic birds are not as robust as penguins even though both are subjected to similar underwater forces (Habib, 2010). Instead, semi-aquatic birds balance the requirements of aerial and underwater flight by changing their flapping behavior; they swim with their wings partially folded, which reduce the force that the wings encounter. In cetaceans (as well as in plesiosaurs and ichthyosaurs) hyperphalangy occurs (Fish, 2004; Storrs, 1993; Motani, 2005), which shapes and supports the flipper. The amount of muscle in the flipper is small and concentrated toward the shoulder, reflecting the restriction of motion

to movements about the shoulder (Fish, 2004; Bannasch, 1994), although limited dorso- and plantar-flexion is still possible. Penguins have much stiffer wings compared to their aerial counterparts: their wing bones are wrapped in connective tissue; their elbows are locked by sesamoid bones; and their feathers are short and stiff (Bannasch, 1994). Sea turtle and sea lion flippers can bend at the elbow but this is primarily for terrestrial locomotion (Fish, 2004). Indeed sea turtle flippers are also wrapped in layers of connective tissue to stiffen the hydrofoil (Fish, 2004; Wynecken, 2001). Lastly, flipper stiffness tends to be higher in fast swimming animals like *Tursiops* (bottlenose dolphin) and lower in slow-swimming, maneuverable animals like *Inia* (river dolphin) (Fish, 2004). Cetacean flukes and dorsal fins are not derived from limbs and are comprised of collagen instead of bone, muscle, and connective tissue (Fish, 2004). Consequently, dorsal fins and especially flukes are not as thick as flippers and are more flexible (Fish, 2004; Fish et al., 2006). The fluke passively deforms during the stroke cycle to produce dorsal camber in the upstroke and ventral camber in the downstroke (Fish et al., 2006). By passively cambering the fluke, lift is generated with a forward component that then thrusts the animal forward.

**Trends in Shape**

The cross-sectional shape of biological hydrofoils varies by taxon and can dynamically change during the stroke cycle (Fish, 2004; Fish et al., 2006). The wings of penguins are asymmetric and possess camber that is dorsally convex (positive camber) (Brannasch, 1994; Fish, 2004) whereas the flippers of pinnipeds are symmetric about the chord and lack camber (Fish, 2004). This means pinniped flippers produce equivalent amounts of thrust during the upstroke and downstroke, while penguin wings produce more thrust in the downstroke

(Brannasch, 1994). However, compared to aerial flying birds the camber of the penguin wing is much reduced and consequently produces more thrust in the upstroke (Brannasch, 1994; Lovvorn, 2001; Fish, 2004). Thus the observed asymmetry of the penguin hydrofoil may be a consequence of its evolutionary history as prior aerial flying birds. Like pinniped flippers, cetacean flippers are symmetric as well but the flippers (and dorsal fin) are primarily involved with stability (Fish, 2004). Instead thrust production is achieved by the fluke (Fish, 2004; Fish et al., 2006; Woodward et al., 2006). At rest (angle of attack = 0) the fluke is symmetrically cambered about the chord (Fish et al., 2006). However, during the upstroke or downstroke of the tail, the flexibility of the cetacean fluke allows it to dynamically change its curvature throughout the stroke cycle, passively taking on an upward or downward oriented camber, respectively (Fish et al., 2006).

Trends in relative AR are reflected in the ecomorphology of birds (O'Keefe, 2001b), whales (Woodward et al., 2006), and dolphins (Fish, 2004). Relatively high AR hydrofoils are associated with animals that have pelagic, cruising lifestyles like *Balaenoptera* (blue whales) (Woodward, et al., 2006) whereas relatively low AR hydrofoils are associated with animals that require greater maneuverability like *Inia* (river dolphins) (Fish, 2004). Furthermore, low AR hydrofoils taper distally forming a triangular shape with a swept back tip consistent with known induced drag-reducing mechanisms (Kuchermann, 1953 and Ashenberg and Weihs, 1984 cited in Fish, 2004).

## PLESIOSAUR HYDROFOIL AND LOCOMOTION

Plesiosaurs swam using two pairs of hydrofoil shaped, hyperphalangic flippers (Storrs, 1993) making them unique among extinct and extant secondarily aquatic tetrapods (Robinson,

1975, 1977; Massare, 1994; Carpenter et al., 2010). Among sauropterygians, the hydrofoil shaped limbs of plesiosaurs are the most specialized for swimming (Godfrey, 1984; Lingham-Soliar, 2000). Among marine reptiles, plesiosaurs and sea turtles are the only ones to swim without using the axial skeleton to generate thrust relying completely on paraxial propulsion (Storrs 1993). Among marine tetrapods, plesiosaurs are the only ones to use two pairs of flippers. Penguins, sea turtles, and otariids (sea lions) have hydrofoil-shaped forelimbs that provide most of the propulsion during swimming (Massare, 1994). In these animals, the hind limbs have different morphologies compared to the forelimbs and functions in steering (Massare, 1994; Godfrey, 1984). Cetaceans and ichthyosaurs also have forelimbs shaped like hydrofoils but propulsion is achieved via dorsoventral (cetaceans) or lateral (ichthyosaurs) flexion of the axial body elements (axial locomotion) instead of through the movement of the limbs (paraxial locomotion) (Cooper et al., 2008; Motani, 2005).

Since plesiosaurs are all extinct and all that is left are their fossilized remains, the exact anatomy of the flipper is impossible to ascertain. However, the cross-sectional and planform shape of the plesiosaur flipper form a clear hydrofoil shape even in the absence of soft tissue (see Wahl et al, 2010 and Figure 5, 6). Intriguingly, the cross-sectional shape of the flippers does not always have dorsally convex curvature (dorsal camber). For instance, the femur of *Callawayasaurus colombiensis* has the opposite, a ventrally convex curvature (ventral camber). This suggests that the hind flippers of this plesiosauromorph produces ventrally directed lift.

The kinematics of individual flippers and the coordination of the fore and hind flippers is an elusive, tantalizing puzzle that has long perplexed plesiosaur paleobiologists (De La Beche and Conybeare, 1821; Watson, 1924; Tarlo, 1957; Robinson, 1975, 1977; Tarsitano and Riess, 1982; Godfrey, 1984; Halstead, 1989; Massare, 1994; Carpenter, 2010; Wahl et al., 2010). At

the heart of this debate is the shape and function of the flippers. The predominant view is that plesiosaur flippers are hydrofoil shaped and functioned to propel the animal by producing lift, similar to how penguins use their wings to fly and soar underwater (De La Beche and Conybeare, 1821; Tarlo, 1957; Robinson, 1975, 1977; Tarsitano and Riess, 1982; Halstead, 1989; Massare, 1994; Carpenter, 2010; Wahl et al., 2010). However, others have argued that

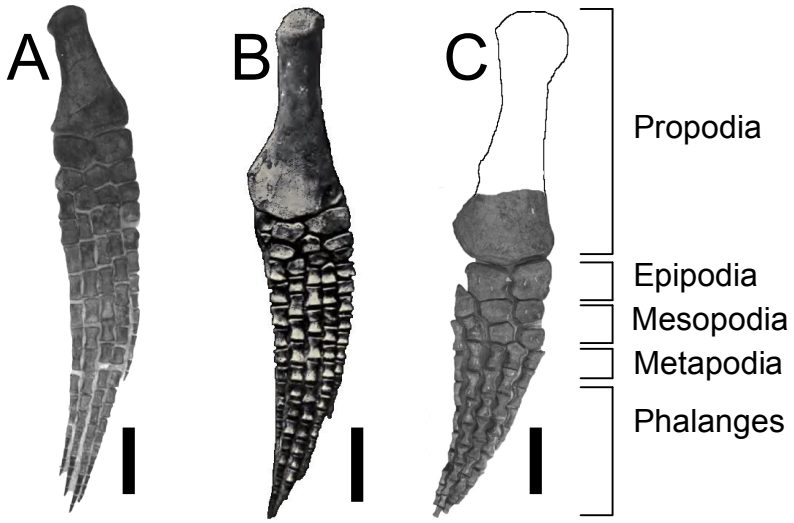


Figure 5. The planform (shape) of plesiosauromorph and pliosauromorph flippers. The bones that make up the limb are labeled. (**A**) Hind limb of *Alzadasaurus kansasensis* (Elasmosauridae, plesiosauromorph). Adapted from Storrs, (1999). Scale bar = 15 cm. (**B**) Hind limb from *Dolichorhynchops osbornii* (Polycotylidae, pliosauromorph). Adapted from Williston (1903). Scale bar = 3 cm. (**C**) Hind limb from *Megalneusaurus rex* (Pliosauridae, pliosauromorph). Adapted from Wahl et al. (2010). Scale bar = 30 cm. Note that plesiosauromorphs flippers are long and narrow while pliosauromorphs are short and wide.

both pairs of flippers were used to push against the water to produce drag-based thrust, similar to how oars or duck feet are used in paddling (Watson 1924). Tarlo (1957) proposed a combination of the two in which the front pair acted as hydrofoils while the back pair acted as oars. However both fore and hind flippers more closely resemble wings than oars in their cross-section and planform (Tarsitano and Riess, 1982; O'Keefe, 2001b; Wahl et al., 2010). Since subaqueous flight puts more constraints on the geometry of a hydrofoil than an oar, both pairs most likely functioned as hydrofoils (Vogel, 1994). This would mean that coordination between fore and hind pairs is crucial. If both pairs produce lift in the same direction (up-up or down-down) then a neutrally buoyant plesiosaur would move upward or downward instead of straight through the water. If the pairs produce lift at opposing directions (up-down or down-up) then a strong pitching moment would be produced around the center of buoyancy that would act to rotate the plesiosaur clockwise or counterclockwise about the pitch axis. Indeed, Carpenter et al. (2010) qualitatively observed that the motion of the fore and hind flippers produces a lot of strain on the trunk of the animal.

Comparison of the planform and cross-sectional shape of plesiosauromorph and pliosauromorph flippers suggest that these morphotypes utilized their flippers differently. For instance, the size of the hind flipper is larger than the fore flipper in pliosauromorphs while in plesiosauromorphs their sizes are more similar (O'Keefe and Carrano, 2005). This suggests that pliosauromorphs compared to plesiosauromorphs likely relied more on the hind limbs for propulsion. Furthermore, work by O'Keefe and Carrano (O'Keefe, 2001b; O'Keefe and Carrano, 2005) has shown that plesiosauromorph and pliosauromorph flipper planform coincides with the hypothesized predation strategy based on known aerodynamic trends. Plesiosauromorphs have high AR wings suggestive of a cruising predatory lifestyle while

pliosauromorphs have low AR wings suggestive of an active pursuit predatory lifestyle (Figure 5) (O'Keefe 2001b). Plesiosaur flippers are also swept back towards the tip (Figure 5) like in cetaceans, an attribute known to reduce induced drag (Kuchermann, 1953 and Ashenberg and Weihs, 1984 cited in Fish, 2004) (Figure 5). Moreover, high-sweep back combined with a low-AR, triangle shaped hydrofoils produce lift at large angles of attack when low-sweep high-AR hydrofoils would fail (Hurt, 1965 cited in Fish, 2004). Pliosauromorphs have high-sweep low-AR flippers (Figure 5) consistent with their hypothesized ecomorphology and maneuverability.

## SUMMARY AND RATIONALE

Plesiosaurs are a group of extinct marine reptiles notable for having two pairs of hydrofoil shaped flippers. These flippers are hydrofoil shaped in cross-section and planform based on the articulation of the flipper bones so they most likely functioned as hydrofoils. Studies on the planform shape suggest that they correlate with hypothesized ecomorphology for the two general morphotypes of plesiosaurs: plesiosauromorphs (long necked, small headed, cruising predators) and pliosauromorphs (short necked, large headed, pursuit predators) (O'Keefe, 2001b; O'Keefe and Carrano, 2005). However, prior to the present study, a quantitative analysis of plesiosaur flippers has not been done, which is necessary in order to (1) understand the hydrodynamic underpinnings of plesiosaur flippers, (2) gain insight into the kinematics of singular and coordinated flipper strokes, and (3) constrain inference about differential optimization in plesiosauromorphs and pliosauromorphs.

# CHAPTER 2: THE SHAPE AND HYDRODYNAMICS OF THE PLESIOSAUR FLIPPER

## INTRODUCTION

Since plesiosaurs are extinct, information about their mode of swimming and the hydrodynamic properties of their flippers must be gleaned from fossil specimens. Soft tissue, which would have added to the functional shape of the hydrofoil, does not usually fossilize and imprints are rarely preserved. The only known imprint of soft tissue associated with a plesiosaur flipper (*Hydrorion brachypterygius* from von Huene, 1923) (Figure 6), suggest that soft tissue extends beyond the posterior edge of the limb forming the hydrofoil trailing edge. Since the function of hydrofoils is tightly linked to its shape (Vogel, 1994), estimating the functional shape of the flipper is extremely important and poses a major obstacle. Indeed, prior to the present study none has directly quantified the hydrodynamic properties of plesiosaur flippers. I present in this study a method for approximating the functional cross-sectional shape of the plesiosaur flipper. A set of plausible shapes based on the outline of the fossil cross-section was obtained mathematically using a combination of curve-fitting and interpolation. These shapes were then evaluated using two-dimensional, steady flow simulations to determine the functionally most effective hydrofoil shape (highest lift-to-drag ratio) for that fossil outline.

Shape strongly determines the function of a hydrofoil. In order to produce net lift, the leading edge has to effectively separate the flow of the fluid such that a pressure difference between the top and bottom surfaces is established and maintained while at the same time reduce flow separation towards the trailing edge, past the maximum thickness of the hydrofoil (Vogel, 1994). This limits the shape of efficient hydrofoils to have a rounded leading edge and a pointed

trailing edge. In biological hydrofoils, hard bone and soft tissue combine to produce this characteristic shape. Their relative contributions vary from the leading edge to the trailing edge. The leading edge is predominantly bone while the trailing edge is predominantly made up of soft tissue (see Figure 6 and also Cooper et al, 2007; Cooper et al., 2008; Fish, 2004; Fish et al., 2006; Fish et al., 2007; Bannasch, 1994; Wynecken, 2001). The leading edge is strengthened by dense bone (Habib, 2010) likely because it has to withstand bending moments during the stroke cycle. Consequently, the shape of the bone at the leading edge closely approximates the shape of the flipper at the leading edge cross-section (Figure 6). Soft tissue envelops the bone but does not obscure its shape. In the same way, the leading edge of fossilized plesiosaur flipper bones would also closely approximate the functional leading edge of the flipper (Figure 6). In contrast to the leading edge, the trailing edge in extant biological hydrofoils is composed predominantly of soft tissue (Figure 6). In cetaceans the trailing edge is composed of dense connective tissue (Figure 6) (Cooper et al., 2008). In penguins, feathers make up part of the trailing edge (Figure 6). The lone instance of plesiosaur flipper soft tissue preservation (von Huene, 1923) (Figure 6) affirms the presence of a trailing edge for plesiosaur flippers and that it extends posterior to the fossil bones. Just how far back the trailing edge extends past a given fossil flipper cross-section is unclear. Since the trailing edge is predominantly soft tissue and very rarely preserved, our approach is to sample the space posterior to the fossil bone for the trailing edge shape that would produce the highest lift-to-drag ratio (L/D) when combined with the fossil outline.

Camber and thickness also affect the properties of the hydrofoil. Increasing camber raises the value of the maximum lift coefficient ($C_{Lmax}$) although the most pronounced increases occur when the camber is small to moderate (Abbott and von Doenhoff, 1959). Raising $C_{Lmax}$ reduces the minimum velocity necessary to produce enough lift to counterbalance drag and

prevent stall (stall speed). Thus hydrofoils with greater camber are effective at slower speeds, which would enable greater maneuverability. As with camber, the thickness of the hydrofoil (Figure 4) affects $C_L$ and $C_D$ (Abbott and von Doenhoff, 1959). In general, increasing thickness raises $C_D$ (Abbott and von Doenhoff, 1959). $C_L$ quickly increases as thickness goes from small to moderate but gradually decreases after that (Abbott and von Doenhoff, 1959).

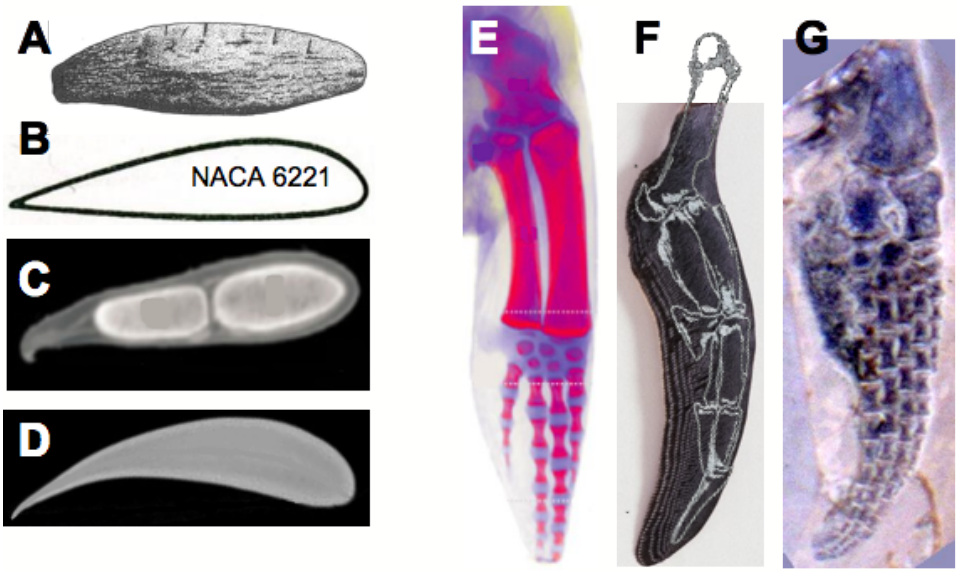


Figure 6. **A**-**B** shows a comparison of the distal cross-section of the *Cryptoclidus femur* (**A**; from Brown, 1981)) to the profile of the NACA 6221 airfoil (**B**), the cross-section of the minke whale foreflipper at the radius and ulna (**C**; from Cooper et al., 2008), and a cross-section of a cetacean fluke (**D**; from Fish et al.; 2006). Soft tissue follows the contour of the minke whale foreflipper until close to the trailing edge (**C**). The cetacean fluke is completely made up of soft tissue (**D**). **E**-**F** shows a comparison of the planform shape of the minke whale foreflipper (**E**, from Cooper et al.; 2008), penguin wing (**F**), and the hind flipper of *Hydrorion brachypterygius* (**G**; from von Huene, 1923). A trailing edge made up of soft tissue extends posterior to the bones in all three foils. Connective tissue makes up the trailing edge in the whale (**E**) while feathers make up the trailing edge in the penguin (**F**).

The angle of attack ($\alpha$) (Figure 4) also determines the value of lift and drag (Vogel, 1994). As $\alpha$ increases, so does lift reaching a maximum value ($C_{Lmax}$) at the critical angle of attack (stall angle) (Vogel, 1994; Abbott and von Doenhoff, 1959). Past this angle, the flow severely separates from the hydrofoil and lift goes down (Vogel, 1994; Webb, 1975; Fish and Battle, 1995). Drag also tends to increase with $\alpha$ (after an initial reduction at low values of $\alpha$) and continues to increase past the stall angle (Vogel, 1994).

The aerodynamic forces of lift and drag depend on the complex interaction of the shape of the hydrofoil (its camber, chord length, and thickness), the physical properties of the fluid (density, velocity, and Reynolds number), and $\alpha$ (Abbott and von Doenhoff, 1959). For the present study, fluid density and velocity are kept constant. The fluid is assumed to have steady flow (stable velocity). Re is set to 10,000,000 (unless otherwise stated) as a simplification in order to avoid the transition between laminar to turbulent flow, which occurs between 500,000 and 1,000,000 as well as reduce the effect of parasitic drag, which is predominant at Re < 500,000 (Vogel, 1994). A fixed value for Re is used since the length of the chord (c) is unknown due to the missing trailing edge (which is presently being reconstructed).

## METHOD

### Inferring Flipper Shape from Fossil Specimens

The exact anatomy of the plesiosaur flipper is impossible to ascertain. However, the cross-sectional and planform shape of the plesiosaur flipper form a clear hydrofoil shape even in the absence of soft tissue (Figure 5, 6) (also see Wahl et al, 2010 and Carpenter, 2010). In plesiosaurs and ichthyosaurs (an unrelated extinct marine reptile) the bony elements of the limbs form a hydrofoil shape in planform (Taylor, 1987) and cross-section. Starting from the distal

end of the propodial (the root of the hydrofoil), the bones assume a hydrofoil shape in cross-section (Figure 6). Undoubtedly, soft tissue surrounded the bones but it stands to reason that the same hydrofoil shape is maintained even when surrounded by soft tissue. It is more parsimonious for the limb to reflect the hydrofoil shaped bone that underlies it than for the bone to evolve a hydrofoil shape only for that shape to be obscured by soft tissue. Assuming the bone does reflect the shape of the functional hydrofoil, then the addition of soft tissue surrounding it would only scale its size and not its shape.

*Specimen*. The following method for determining the functional flipper hydrofoil shape was applied to the femur and humerus of *Cryptoclidus eurymerus*, HMG V1104 (figured in Brown, 1981; presented again in Figure 9 below).

*Image pre-processing*. The cross-section of each propodial was obtained via end-on distal view photographs. The resulting silhouette of the propodial at its widest section was taken as the cross-sectional shape for that propodial. The photographs used were obtained directly or indirectly through published photographs of the propodials. The fossil silhouettes were reduced to single pixel outlines then converted to x,y-coordinates using the Pathfinder macro in ImageJ (NIH ImageJ, Rasband 1997-2012). The outline was divided into the top and bottom curves using the anterior-most and the posterior-most points as boundaries. The anterior end (fossil leading edge) and posterior end (fossil trailing edge) of the outline were then examined for an abrupt change in curvature as this signals the point at which the outline of the fossil bone no longer traces the top or bottom surfaces of the hydrofoil. Coordinates past this point would not contribute to the functional shape of the hydrofoil and were removed.

*Estimating the leading edge*. In order to recreate the rounded leading edge of the hydrofoil, a circle was fitted to the anterior end of the propodial tangent to the lines connecting

the remaining two anterior-most coordinates each of the top and bottom curves. The arc of the circle that extended anteriorly and connected the top and bottom curves was used in place of the original anterior fossil outline. This substitution was necessary in order to correct for any wear in the fossil or other breaks in the outline of the leading edge. The arc of the fitted circle usually only slightly extended past the original fossil trailing edge.

*Estimating the trailing edge.* In contrast to the leading edge, the process of approximating the size and shape of the trailing edge is comparatively more involved (Figure 8). In order to parameterize the fossil outline and smooth out any irregularities, a polynomial was fitted to the top and bottom surfaces separately. For this, I used the Class Shape Transformation (CST) parameterization method specifically developed by Kulfan and Bussoletti (2006) (see also Lane and Marshall, 2009) to formulate the polynomial that best fits a given set of points that define an air/hydrofoil shape. This powerfully simple method could model a wide array of shapes with a small number of equations and parameters (Kulfan and Bussoletti, 2006; Lane and Marshall, 2009). The equations are the same as the Bezier curve equations with an added class function term (equation 1 to 3 below) (Kulfan and Bussoletti, 2006; Lane and Marshall, 2009). The class function term (equation 1 below) specifies a base or standard shape category from which is derived all other shapes in that category (Kulfan and Bussoletti, 2006). This term also reduces the number of coefficients necessary to parameterize the curve since the base shape that is closest to the air/hydrofoil modeled could be chosen before the coefficients are set (Kulfan and Bussoletti, 2006). The class function term is molded and transformed into the desired shape by the shape function (equation 2 below), which is defined by a Bernstein Polynomial (Kulfan and Bussoletti, 2006). The resulting fitted curves are smooth and do not suffer from the same degree of oscillation problems that results from other parameterization methods such as B-Splines and

NURBS (Lane and Marshall, 2009). For a hydrofoil with a rounded leading edge and pointed trailing edge, the class function, $C(\psi)$, is given by

$$C(\psi) = \sqrt{\psi}(1-\psi)^1 \tag{3}$$

where $\psi = \frac{x}{c}$, x is the x-coordinate and $c$ is the length of the chord of the hydrofoil (Figure 4).

The general form of the shape function, $S(\psi)$, is given by

$$S(\psi) = \sum_{r=0}^{n} \frac{n!}{r!(n-r)!} A_r \psi^r (1-\psi)^{n-r} \tag{4}$$

where $\frac{n!}{r!(n-r)!}$ is the binomial coefficient, $n$ is the order of the Bernstein Polynomial, and $A_r$ is the coefficient to be set using least-squares fitting. Combining the two equations yield the general equation below for the function, $Z(\psi)$, of a parameterized hydrofoil with a rounded leading edge and pointed trailing edge

$$Z(\psi) = \sqrt{\psi}(1-\psi) \sum_{r=0}^{n} \frac{n!}{r!(n-r)!} A_r \psi^r (1-\psi)^{n-r} \tag{5}$$

For this study, a Bernstein Polynomial of order three (n = 3) was used for the top and bottom curves since Bernstein Polynomials (n = 1 and 2) visibly fail to fit the outline of the fossil. The

expanded CST parameterization equation for a third order Bernstein Polynomial is given below for the top curve

$$Z(\psi)_{top} = \sqrt{\psi}(1-\psi)\ \left(A_1(1-\psi)^3 + A_2(1-\psi)^2\psi + A_3(1-\psi)\ \psi^2 + A_4\psi^3\right) + \psi\Delta z_{top} \quad (6)$$

and the bottom curve

$$Z(\psi)_{bottom} = \sqrt{\psi}(1-\psi)\left(A_1(1-\psi)^3 + A_2(1-\psi)^2\psi + A_3(1-\psi)\ \psi^2 + A_4\psi^3\right) + \psi\Delta z_{bottom} \quad (7)$$

where $\Delta z_{top} = \frac{z_{TE,top}}{c}$ is the thickness of the trailing edge tip for the top ($z_{TE,top}$) normalized to the length of the chord (Figure 4) and $\Delta z_{bottom} = \frac{z_{TE,bottom}}{c}$ is the thickness of the trailing edge tip for the bottom ($z_{TE,bottom}$) also normalized to the length of the chord. For this study, the thickness of the trailing edge tip was one pixel, thus a value of zero was used. The polynomial was fitted to the points defining the fossil outline by determining the appropriate coefficients ($A_1$ to $A_4$) using least-squares fit via the `lsqnonlin` command from the optimization toolbox in MATLAB.

In order to estimate the shape of a candidate trailing edge for the fossil outline, a point was chosen posterior to the fossil to serve as the tip of the trailing edge (the point where the top and bottom surfaces of the candidate trailing edge meet) (Figure 8). This point together with the posterior end of the fossil forms a candidate trailing edge for the fossil hydrofoil. The parameterized top and bottom curves were then interpolated to this point via shape-preserving piecewise cubic Hermite interpolation (pchip) (Moler, 2004; Fritsch and Carlson, 1980). The top and bottom curves were parameterized and interpolated separately then later recombined. This

interpolation was selected for its balance of smoothness and shape preservation (local monotonicity). Full degree (global) interpolation does not preserve shape since it tends to vary widely between points. On the other extreme, piecewise linear interpolation preserves shape but lacks any smoothness. In between these two extremes are piecewise cubic spline interpolation and shape-preserving cubic Hermite interpolation. Piecewise cubic spline interpolation preserves shape better than full degree interpolation and is smoother than piecewise linear interpolation but does not guarantee shape preservation (Moler, 2004). Indeed, piecewise cubic spline interpolation tended to overshoot the y-value of the trailing edge tip within the gap between the posterior-most edge of the fossil outline and the tip. On the other hand, shape-preserving piecewise Hermite interpolation guarantees local monotonicity, which means that the interpolated curve does not overshoot the trailing edge tip. However, it does so at the cost of breaks in the second derivative (the first derivative is still continuous) whereas cubic spline interpolation is continuous at the second derivative as well as the first. In other words, shape-preserving cubic interpolation guarantees local monotonicity but is not as smooth as cubic spline interpolation. For this study, shape-preserving piecewise cubic Hermite interpolation was performed using the `pchip` option in the `interp1` command in MATLAB.

At extreme trailing edge tips such as those too far posterior from the fossil outline, the interpolated top and bottom trailing edge curves may intersect or overlap within the gap between the fossil and the tip (Figure 8). Such instances produce hydrofoils that are beyond the reasonable bounds of what is plausible biologically and reflect the limits of plausible shapes as constrained by the top and bottom curvatures of the fossil outline. To circumvent this natural limit and still evaluate the hydrofoil that would correspond to this trailing edge tip, I replaced this trailing edge with the closest trailing edge whose tip falls along the same y-value (different

x-value) but that did not intersect or overlap. Prior to attachment, the replacement tip was stretched along the x-axis such that it and the original tip being tested now have the same endpoint x-value. The result was a mosaic hydrofoil with a stretched trailing edge (tail) that is no longer fully constrained by the curvature of the top and bottom surfaces of the fossil. The entire process from CST curve fitting through piecewise cubic interpolation and stretching was performed through a custom MATLAB script that I generated (see Appendix 1).

The lift and drag of each complete hydrofoil (fossil outline + simulated trailing edge) was determined using XFoil version 6.94, an airfoil simulation and design program (Drela, 1989; Drela and Giles, 1987). XFoil models the flow streams around the hydrofoil and the wake using a coupled viscous-inviscid panel method (Drela, 1989) given the following: the coordinate file of hydrofoil, the Reynolds number (Re), Mach number (set to M=0), and $N_{crit}$, which determines where the transition laminar to turbulent flow transition occurs (set to $\tilde{n} = 9$). This method used will only be briefly described here; for the detailed derivation see Drela and Giles (1987), Drela (1989a, b), and Youngren (2001). In order to determine the flow around the hydrofoil, XFoil divides the outline of the flipper and the wake into discrete panels (120 max), calculates the potential flow around each panel, and then combines them to simulate the flow stream (Drela, 1989; Fearn, 2008). The flow around each panel is simulated using the superposition of the freestream flow, a vortex distribution over the hydrofoil, and a source distribution over the hydrofoil and wake. Altogether this forms a linear-vorticity streamfunction ($\Phi$), given by

$$\Phi(x,y) = u_\infty y - v_\infty x + \frac{1}{2\pi}\int \gamma(s)\ln r(s;x,y)ds + \frac{1}{2\pi}\int \sigma(s)\alpha(s;x,y)ds \qquad (8)$$

$$\text{and} \quad \phi(x,y) = \frac{1}{2\pi}\int \gamma(s)\ln r(s;x,y)ds + \frac{1}{2\pi}\int \sigma(s)\alpha(s;x,y)ds \tag{9}$$

where γ is the strength of the vortex distribution, σ is the strength of the source distribution, *x,y* denotes a point on the flow field, *s* is a point along the panel, and *r* is the magnitude of the vector between the points *x,y* and *s* with angle α; $u_\infty$ $(= q_\infty \cos\alpha)$ and $v_\infty$ $(=q_\infty \sin\alpha)$ are components of the freestream velocity ($q_\infty$). The coefficient of pressure ($C_P$) could then be approximated from (8) and (9) using

$$C_p \approx -2\frac{\partial \phi / \partial x}{q_\infty} \tag{10}$$

The coefficient of lift ($C_L$) is directly calculated by integrating the pressure distribution around the entire hydrofoil,

$$C_L = \oint C_p d\bar{x} \tag{11}$$

where $\bar{x} = x\cos\alpha + y\sin\alpha$. The coefficient of drag ($C_D$) is estimated by applying the Squire-Young formula and evaluating the last point in the wake (≥ 1 chord length downstream):

$$C_D = 2\theta(u_{edge}/q_\infty)^{(H+5)/2} \tag{12}$$

where $u_{edge}$ is the flow velocity at the edge of the boundary layer and *H* is the shape parameter.

In order to simulate viscous conditions, Xfoil address the inherent assumptions and simplifications of the panel method, which is: the viscosity of the fluid is neglected, the flow field has no vorticity, the flow is incompressible, and that the flow over the top and bottom surfaces leave the trailing edge smoothly (Kutta condition) (Fearn, 2008). Fluid viscosity affects the tendency of the flow to separate from the surface of the hydrofoil creating a boundary layer of some thickness ($\theta$). Flow about the hydrofoil now goes over the edge of this boundary layer, effectively changing the shape of the hydrofoil. XFoil address this effect by applying the panel method to the edge of boundary layer instead of the hydrofoil surface. It calculates the 2-dimensional edge of the boundary layer using the following standard compressible integral equations for the momentum thickness (boundary layer thickness, $\theta$) and kinetic energy shape parameter ($H^*$):

$$\frac{d\theta}{d\xi} + \left(2 + H - M_{edge}\right)\frac{\theta}{u_{edge}}\frac{du_{edge}}{d\xi} = \frac{C_f}{2} \tag{13}$$

$$\theta\frac{dH^*}{d\xi} + \left(2H^{**} + H^*(1-H)\right)\frac{\theta}{u_{edge}}\frac{du_{edge}}{d\xi} = 2C_{dissipation} - H^*\frac{C_f}{2} \tag{14}$$

where $\xi$ is the boundary layer coordinate, $M_{edge}$ is the Mach number at the edge of the boundary layer ($M_{edge} = 0$ throughout this study), $u_{edge}$ is the velocity at the edge of the boundary layer, $C_f$ is the skin-friction coefficient, $C_{dissipation}$ is the dissipation coefficient, $H$ is the shape parameter, and $H^{**}$ is the density shape parameter. The following dependencies in functional notation are assumed in order to evaluate equations (13) and (14):

$$H^* = H^*(H_k, M_{edge}, Re_\theta) \tag{15}$$

$$H^{**} = H^{**}(H_k, M_{edge}) \tag{16}$$

$$C_f = C_f(H_k, M_{edge}, Re_\theta) \tag{17}$$

$$C_D = C_D(H_k, M_{edge}, Re_\theta) \tag{18}$$

where $Re_\theta$ is the Reynolds number multiplied by the boundary layer thickness ($\theta$). The specific expressions are given in Drela and Giles (1987). Another simplification inherent to the panel method is that the flow field does not have any vorticity (the curl of the velocity field is assumed to be zero). Turbulent flow affects the thickness of the boundary layer differently from laminar flow. XFoil address this by calculating the above dependencies (15, 16, 17, 18) for laminar and turbulent flows then switching from between those expressions at the transition point. In order to do so, XFoil determines where this transition occurs by modeling the growth of the amplitude of the largest Tollmien-Schlichting wave ($\tilde{n}$) using the equation below:

$$\frac{d\tilde{n}}{d\xi} = \frac{d\tilde{n}}{d\mathrm{Re}_\theta}(H_k)\frac{d\mathrm{Re}_\theta}{d\xi}(H_k,\theta) \tag{19}$$

The transition is *assumed* to occur when the preset value for $\tilde{n}$ is met. In the present study, the standard value of $\tilde{n} = 9$ is used throughout. To account for the compressibility of flow, XFoil uses the Karman-Tsien correction, which depends on the Mach number. However, for the present study, the Mach number is set to zero (M = 0) so this correction does not apply and the assumptions is made that the flow is incompressible. Since the fluid medium for the present study is water (essentially incompressible under normal conditions) and the flow speed is low,

this is a valid assumption. Finally, XFoil assumes that the flow over the top and bottom surfaces leaves the trailing edges moothly (Kutta condition).

XFoil calculates the solution to the streamfunction and boundary conditions using the linear algebra and the Newton-Raphson method (Drela and Giles, 1987; Drela, 1989). Starting with an estimate of the value of the solution, successive iterations are made using solutions from the preceding iteration until the answer is obtained by convergence or until the maximum number of iterations is reached. For the present study, the maximum number of iterations is set to 300. If XFoil fails to converge to an answer, a L/D value of zero is assigned to that airfoil.

A set of complete hydrofoil shapes (fossil outline + candidate trailing edge) with different trailing edge shapes were evaluated using XFoil. The trailing edge tip was used to determine the shape of the trailing edge via interpolation from the posterior end of the fossil outline (see above). The location of the trailing edge tip is determined by sampling the x,y-coordinate space posterior to the fossil at coarse (5% of the cross-sectional length of the fossil element) and fine intervals (1% of cross-sectional length) (Figure 9). The x,y-coordinate of the leading edge of the fossil outline is set to (0,0) and the rest of the fossil element is scaled to span the x-coordinates from 0 to 1. The L/D ratio is obtained using XFoil for each completed hydrofoil shape (fossil outline + candidate trailing edge) at various angles of attack (usually from -10º to +10º at 0.25º increments). This range is usually sufficient to determine the angle of attack with the maximum L/D. A Re value of 10,000,000 is used to test the hydrofoil shapes. This Re value is within the range of Re experienced by cetaceans, large marine animals comparable to plesiosaurs (Fish, 1993). This value was chosen in order to avoid the transition from laminar to turbulent flow which would occur at Re between 500,000 and 1,000,000. The sign of L/D depends on which side has the lower pressure (dorsal or ventral side of the hydrofoil) with the dorsal side given a

positive (+) sign and the ventral side given a negative (-) sign. The L/D value for each candidate hydrofoil is plotted on the z-axis with the x,y-coordinate of the corresponding trailing edge tip plotted on the x,y-plane. This produces a 3-D contour plot of the sample space for a particular angle of attack. The largest lift-to-drag ratio (L/D) for the complete hydrofoil (fossil outline + candidate trailing edge) was used as criterion to determine the best functional trailing edge for the fossil element among the set of candidates.

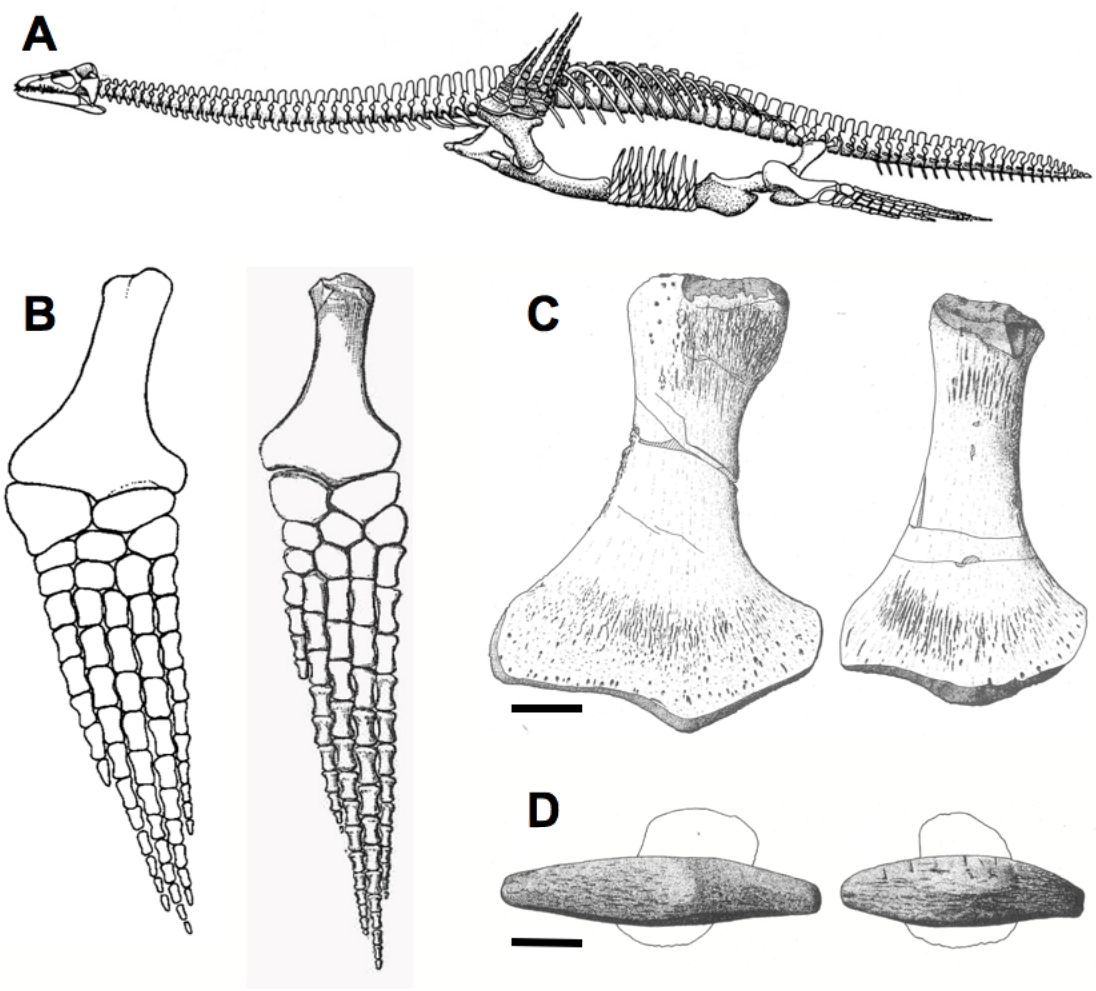


Figure 7. The skeletal reconstruction of *Cryptoclidus eurymerus* is shown in **A** (from Brown, 1981). The planform of the fore flipper (from Storrs, 1993) and hind flipper (modified from Andrews, 1913) are shown from left to right, respectively, in **B**. The humerus and femur (from Brown, 1981) are shown from left to right, respectively, in **C**. The distal cross-section of the femur and humerus (from Brown, 1981) are shown from left to right, respectively, in **D**. Both scale bars are 5 cm. Note how the humerus angles forward from the base (**B**) and how rest of the flipper from the radius and ulna makes a sharp angle backward.

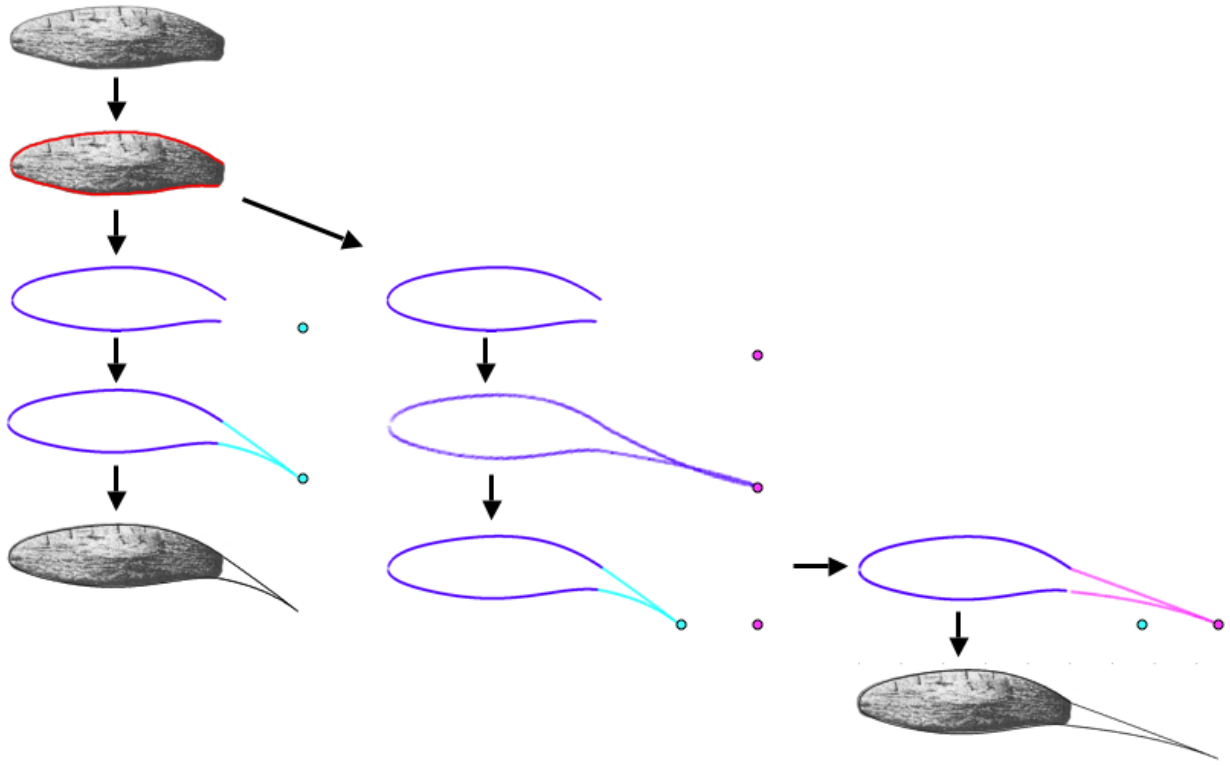

Figure 8. Flow chart of the steps involved in creating the shape for the complete hydrofoil. Briefly, (from the left column top to bottom) the outline of the surface of the hydrofoil (in red) is parameterized by curve-fitting (in blue). A point is selected posterior to the fossil outline to serve as the trailing edge tip. The fossil outline is then interpolated to this point filling the gap in between (in cyan) and the hydrofoil is constructed. If the interpolation results in the top and bottom curves crossing within this gap (center of the middle column), the trailing edge is removed and replaced with the closest trailing edge with the same x-coordinate that did not cross. This trailing edge is then stretched such that the stretched tip reaches the desired trailing edge tip (last column, in magenta).

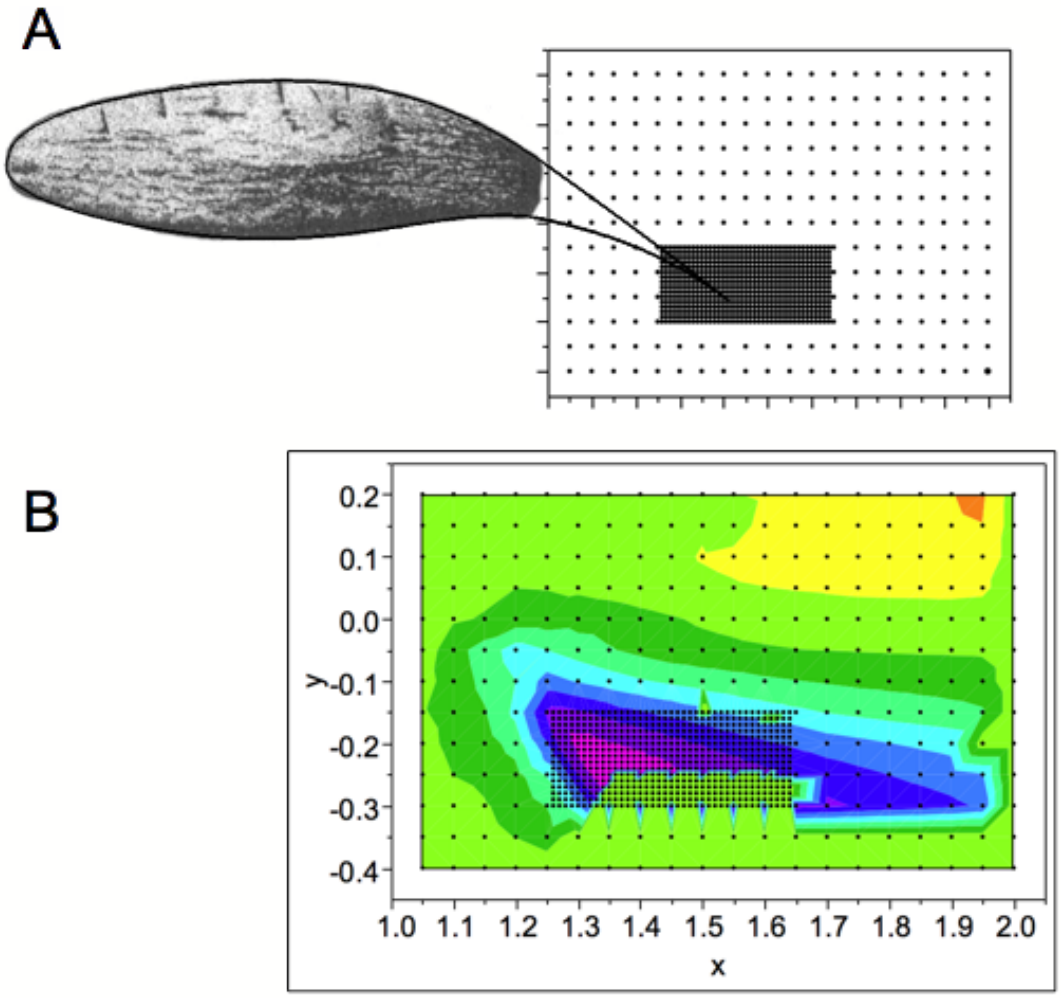


Figure 9. Sample contour plot showing the position of the trailing edge tips and corresponding L/D values. The x,y-coordinate plane posterior to the fossil element, in this case, the femur of *Cryptoclidus eurymerus* (**A**) from Brown (1981) was sampled for the location of the trailing edge tip that, together with the fossil outline, would produce the functionally best performing hydrofoil shape. For coarse sampling the points are spaced apart by 5% of the length of the fossil. For fine sampling this space is reduced to 1% of the length of the fossil. Shown in (**B**) is the resulting contour plot at angle of attack ($\alpha$) of 2.25º. The L/D obtained through XFoil for each hydrofoil is plotted with the x,y-coordinate of the tip on the x,y-plane. Cool colors denote high magnitude lift generated from the dorsal side (positive L/D), termed "dorsal lift". Hot colors denote high magnitude lift generated from the ventral side (negative L/D ratio), termed "ventral lift".

## RESULTS

*C. eurymerus* Femur Hydrofoil

The 2-D functional hydrofoil shape was reconstructed for the distal cross-section of the *C. eurymerus* femur from specimen HMG V1104, figured in Brown (1981) (Figure 7). The contour plots for the set of candidate hydrofoil shapes for the femur is shown in Figure 10 for the range of angle of attack ($\alpha$) from -8º to +8º. The plots shown here is only a subset of the full range of angles of attack examined ($\alpha$ from -10º to +10º at 0.25º increments). Highlighted in magenta in Figure 10 are the shapes with L/D (= $C_L/C_D$) values within the top 5%. This region of high positive L/D values (positive because lower pressure is on the dorsal side of the hydrofoil) first appears around 0º, peaks by +2º, and disappears again by +4º (Figure 10, Table 2). At $\alpha$ below +2º the ventral side of the hydrofoil produces lift and a negative L/D value is obtained. Highlighted in red in Figure 10 are the shapes with L/D values within the bottom 5%. The peak range of ventral directed lift ("ventral lift") is attained by $\alpha$ = -2º (max L/D = -126), which persists and expands beyond $\alpha$ = -8º. Indeed, this plateau persists past $\alpha$ = -10º and only starts to wane past $\alpha$ = -15º. This is in stark contrast to the relatively short-lived but high magnitude "dorsal lift" (max L/D = 308).

The reconstructed hydrofoil shape of the *C. eurymerus* femur is shown in Figure 11. This hydrofoil shape is among the shapes that most consistently produced L/D values in the top 5% across the range of $\alpha$ where the top 5% L/D values occur ($\alpha$ = -0.75º to 3.75º). Additionally, the x,y-coordinate of its trailing edge tip is the spacial mean of the x,y-coordinates of the trailing edge tips of these hydrofoils. The reconstructed trailing edge comprises about 26% of the overall hydrofoil shape based on the x-coordinate of the trailing edge tip (Figure 11, Table 2). This produces a chord length of about 0.24 m and a maximum camber of about 11% (relative to chord

length) located at 36% of the chord length from the leading edge (Figure 11, Table 2). The corresponding plots of $C_L$ vs $\alpha$, $C_D$ vs $\alpha$, and L/D vs $\alpha$ for the reconstructed hydrofoil shape are shown in Figure 11 (B-D respectively). Their values are obtained through XFoil. The Re used was calculated using Equation 1 (see above) from the chord length of the reconstructed hydrofoil shape and assuming a flow velocity of 1 m/s (the swim speed estimate by Motani, 2002). Together with the kinematic viscosity of water ($\eta = 1.0x10^{-6}$ $m^2/s$), the Re value used was 240,000. The highest value of lift ($C_{Lmax}$) obtained at this Re value is 2.02 at $\alpha = 26.75^o$ (Figure 11, Table 2). This $\alpha$ is also known as the stall angle since the value of $C_L$ drops drastically past this $\alpha$. The lowest value of drag ($C_{Dmin}$) is 0.042 and occurs at -11.75º (Figure 11, Table 2). The maximum value of the lift to drag ratio (max L/D) is 16.52 and occurs at $\alpha = 13.25^o$.

*C. eurymerus* Humerus Hydrofoil

The 2-D functional hydrofoil shape was reconstructed for the distal cross section of the *C. eurymerus* humerus from specimen HMG V1104, figured in Brown (1981) (Figure 7). The contour plots obtained for the set of candidate hydrofoil shapes for the *C. eurymerus* humerus is shown in Figure 12 for $\alpha$ from -8º to +8º. As with the femur, the range of $\alpha$ shown here is only a subset of the full range examined (-10º to +10º at 0.25º increments). (These contours are stacked, in order, to form a movie, see Supplemental Figure S2). The top and bottom 5% are highlighted in magenta and red respectively. The top 5% L/D values are centered around $\alpha = 0^o$ with a the highest value at $\alpha = 0.75^o$ (max L/D = 223). The bottom 5% appears around $\alpha = -4^o$, peaks at $\alpha = -8^o$ (max L/D = -134) and continues past $\alpha = -10^o$.

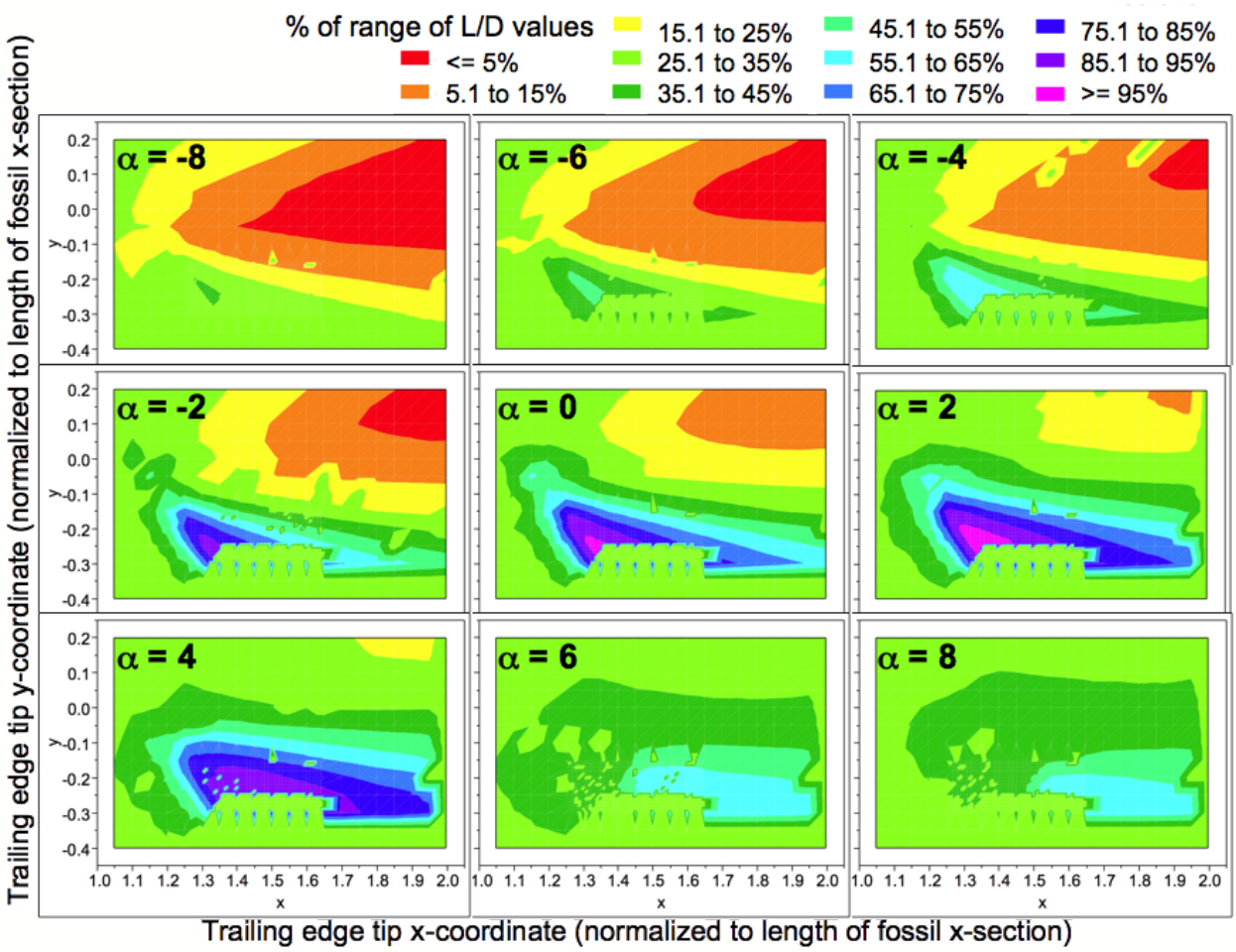


Figure 10. Contour plots for the *C. eurymerus* femur for α from -8º to +8º. The x,y-coordinates of the trailing edge tip is plotted on the x,y-plane with the magnitude of the L/D resulting from the corresponding completed hydrofoil (trailing edge + fossil outline) plotted as contours. Cool colors denote dorsal oriented lift (max L/D = 308) and hot colors denote ventral oriented lift (max L/D = -126). In magenta are the shapes with L/D values within the top 5%. In red are the shapes with L/D values within the bottom 5%.

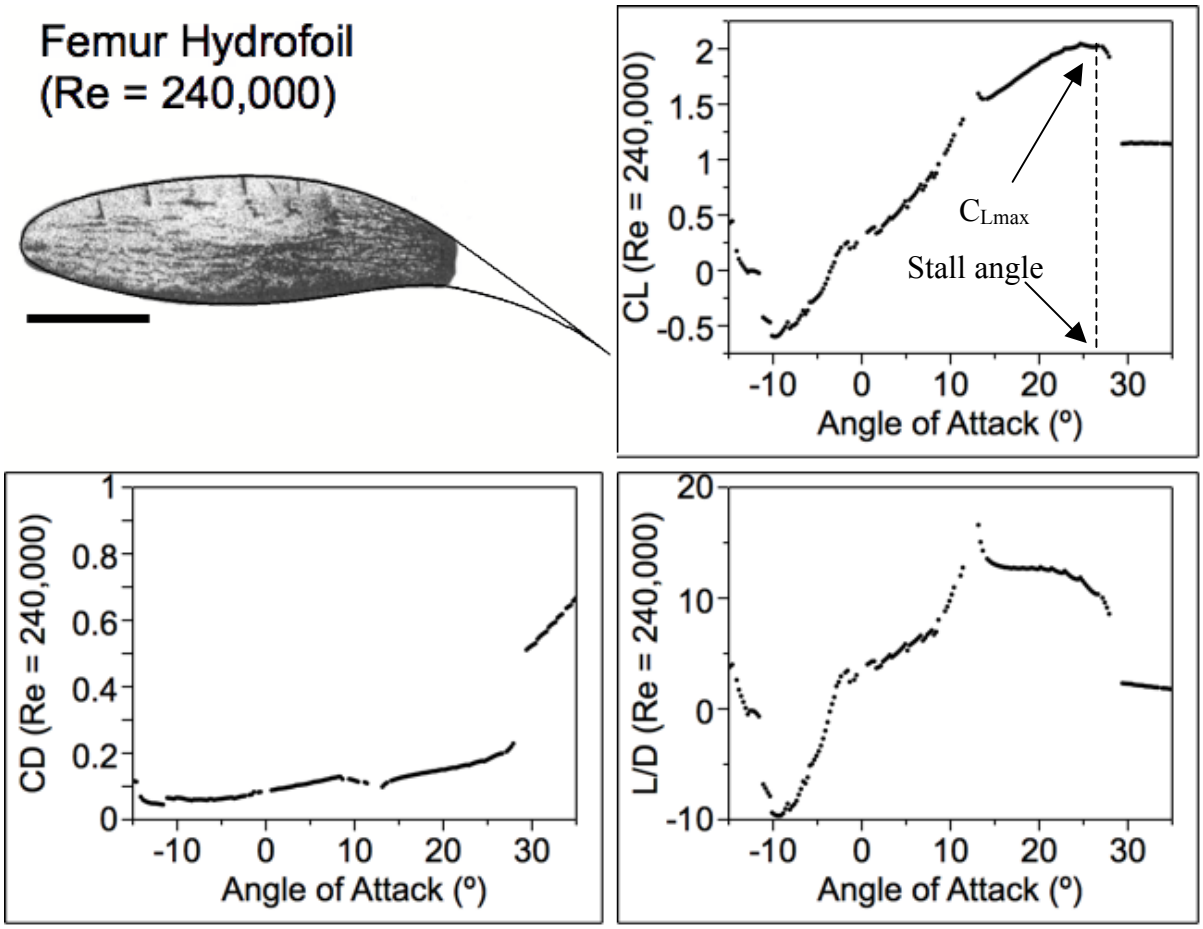


Figure 11. The reconstructed hydrofoil shape for the *C. eurymerus* femur (**A**). Shown in **B**-**D**, respectively, are the plots of $C_L$ vs $\alpha$, $C_D$ vs $\alpha$, and L/D vs $\alpha$ using Re = 240,000.
Scale bar = 5 cm.

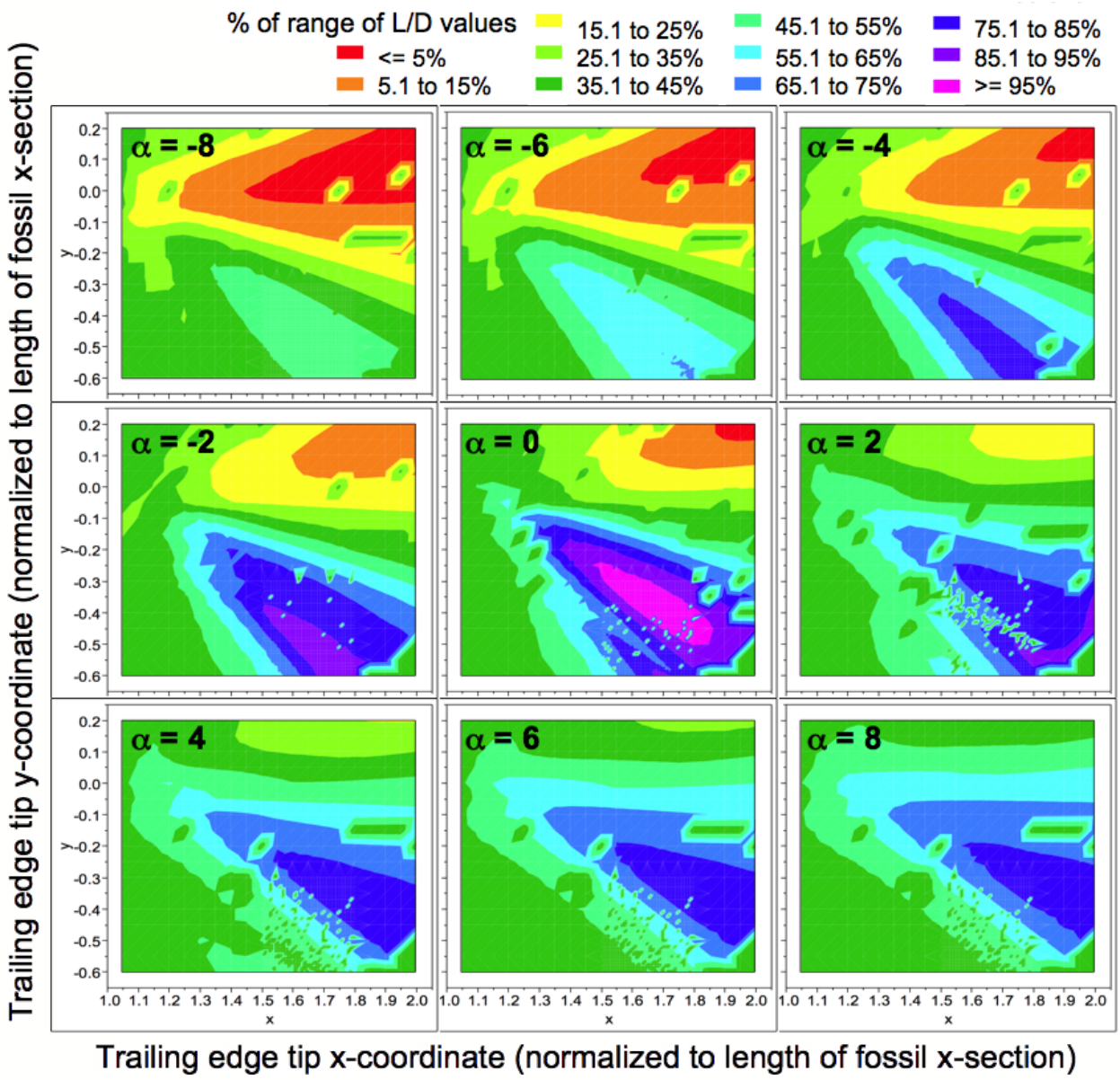


Figure 12. The contour plots for the *C. eurymerus* humerus for α from -8º to +8º, plotted as in Figure 10. Cool colors denote dorsal oriented lift (max L/D = 223) and hot colors denote ventral oriented lift (max L/D = -136). In magenta are the shapes with L/D values within the top 5%. In red are the shapes with L/D values within the bottom 5%.

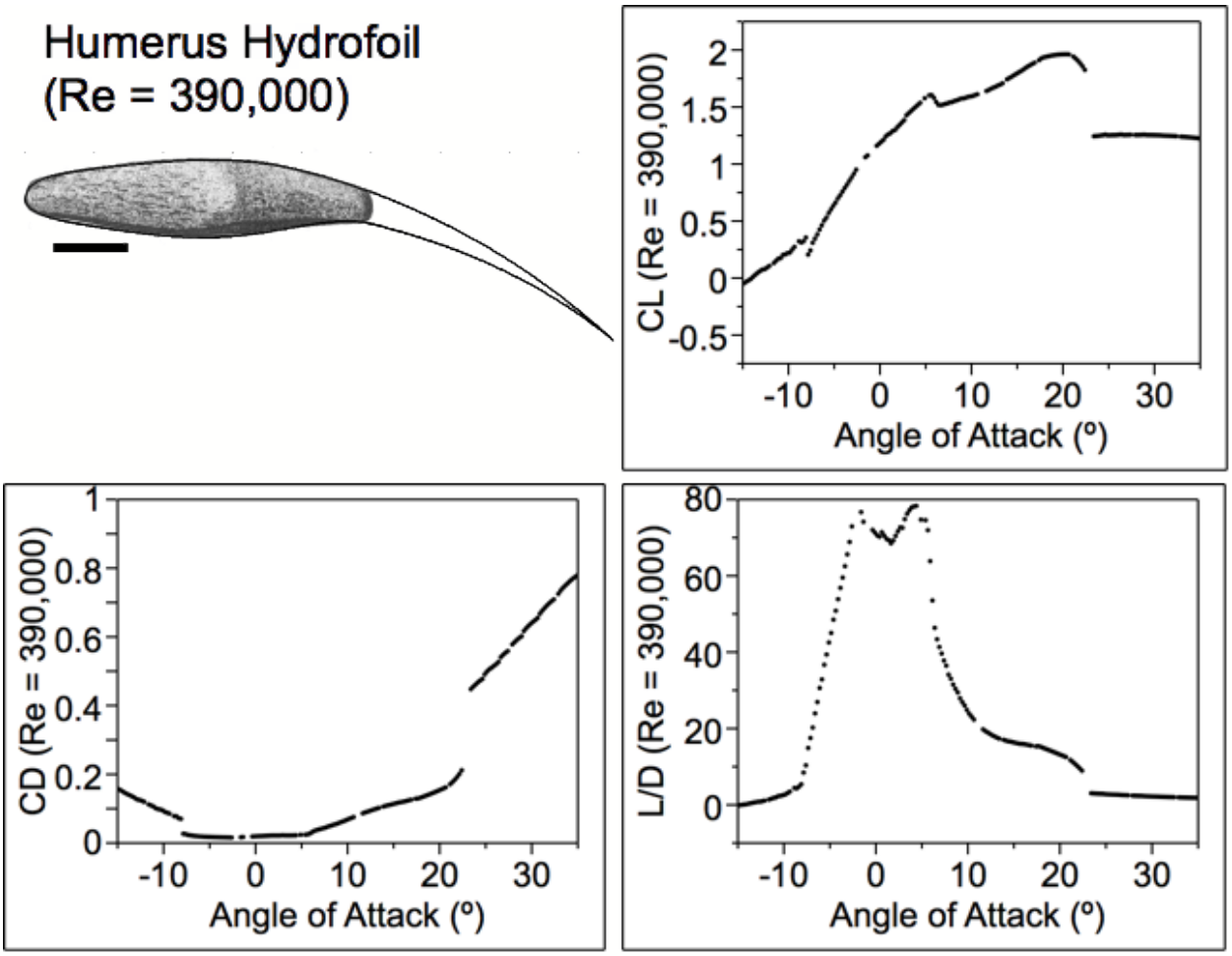


Figure 13. The reconstructed hydrofoil shape for the *C. eurymerus* humerus is shown in **A**. Shown in **B**-**D**, respectively, are the plots of $C_L$ vs $\alpha$, $C_D$ vs $\alpha$, and L/D vs $\alpha$ using Re = 390,000. Scale bar = 5 cm.

The reconstructed hydrofoil shape of the *C. eurymerus* humerus is shown in Figure 13. This hydrofoil shapes is among those that most consistently produced L/D values in the top 5% across the range of $\alpha$ where the top 5% occur (-1.75º to 1.75º). Its trailing edge tip x,y-coordinate also corresponds to the spacial mean of the x,y-coordinates of these hydrofoils. The reconstructed trailing edge soft tissue for the humerus comprises about 43% of the entire hydrofoil shape based on the x-coordinate of the trailing edge tip (Figure 13, Table 2). This

produces a chord length of about 0.39 m and a maximum camber of 11% (relative to chord length) located at 54% of the chord length from the leading edge (Figure 13, Table 2). The corresponding plots of $C_L$ vs $\alpha$, $C_D$ vs $\alpha$, and L/D vs $\alpha$ for the reconstructed hydrofoil shape are shown in Figure 13 (B-D respectively). The Re (= 390,000) used was calculated from the chord length of the reconstructed hydrofoil shape and assuming a flow velocity of 1 m/s (Motani, 2002). At this Re, the reconstructed humerus hydrofoil attains $C_{Lmax}$ = 1.95 at $\alpha$ = 20.5, $C_{Dmin}$ = 0.013 at $\alpha$ = -2.5º, and max L/D = 78.0 at $\alpha$ = 4.15º (Figure 13, Table 2).

In order to further characterize the hydrodynamic properties of the reconstructed hydrofoils, they were compared to engineered hydrofoils that have similar shapes, the Wortmann FX 63-137 (Althaus and Wortmann, 1981) and NACA 63(3)-618 (Figure 14, Table 2). Since the original Wortmann FX 63-137 airfoil coordinates were not analytically smooth (Selig and McGranahan, 2004), the airfoil coordinates used in this study are those that have been previously smoothed out (Selig and McGranahan, 2004). The *C. eurymerus* humerus hydrofoil and the Wortmann FX 63-137 airfoil have similar maximum thickness, location of maximum thickness, and location of maximum camber (Figure 14, Table 2). However, the maximum camber for the humerus hydrofoil is 11% while for the Wortmann FX 63-137 airfoil it is only 6% (Figure 14, Table 2). Under the same Re (= 390,000), both foils attained similar values for $C_{Lmax}$, $C_{Dmin}$, and stall angle (Table 2). However, the Wortmann FX 63-137 airfoil has a larger maximum L/D value (115.8 vs 78.0 for the humerus hydrofoil; see Table 2).

The NACA 63(3)-618 airfoil and *C. eurymerus* femur hydrofoil have similar maximum thickness and location of maximum thickness (Table 2). However, the femur hydrofoil has a larger maximum camber (11% vs 3% for the NACA 63(3)-618) airfoil that is located further back (63% vs 50% for the NACA 63(3)-618). Under the same Re (= 240,000), the femur

hydrofoil attained higher $C_{Lmax}$ and $C_{Dmin}$ values but lower maximum L/D compared to the NACA 63(3)-618 airfoil. The stall angle for the femur hydrofoil is slightly larger at 26.75º compared to 20.5º for the NACA 63(3)-618 airfoil.

The reconstructed *C. eurymerus* hydrofoils were also compared to published values of $C_L$ at $\alpha = 10º$ under inviscid conditions (Table 3) for various cetacean taxa (Fish et al., 2007) as well as the Wortmann FX 63-137 airfol, the NACA 63(3)-618 airfoil, and the NACA 0021 airfoil, which has no camber and, thus, is symmetric about the chord. The *C. eurymerus* hydrofoils and the similarly shaped engineered hydrofoils (Wortmann FX 63-137 airfol and the NACA 63(3)-618 airfoil) had noticeably higher $C_L$ values (Table 3) compared to the cetacean fluke hydrofoils and the NACA 0021 airfoil.

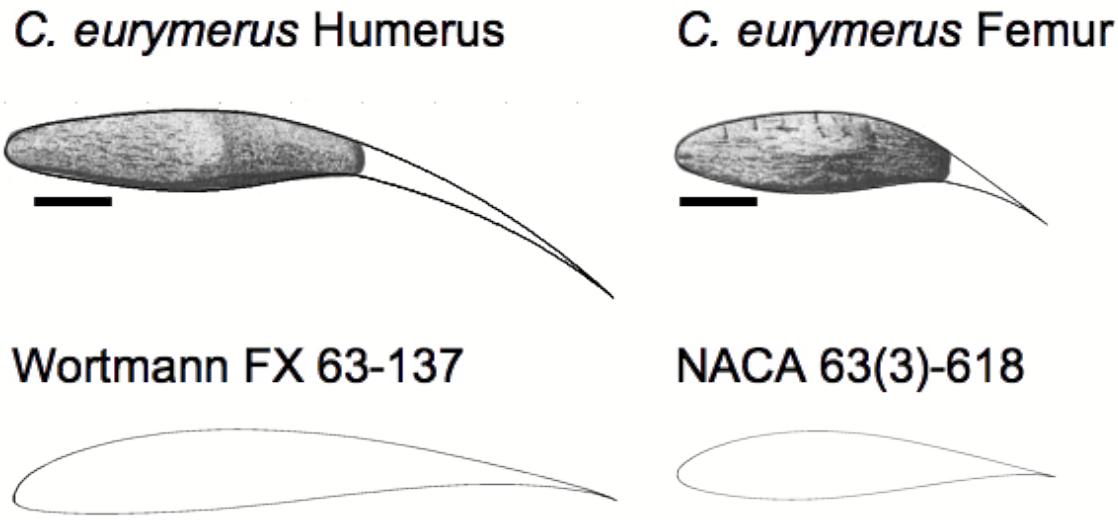


Figure 14. The reconstructed *C. eurymerus* humerus and femur hydrofoils with similarly shaped engineered airfoils. Scale bar = 5 cm.

Table 2: Geometric and hydrodynamic properties of the *C. eurymerus* femur and humerus compared to engineered airfoils with matched Re.

| | ***C. eurymerus* Humerus** | ***C. eurymerus* Femur** | **Wortmann FX 63-137** | **NACA 63(3)-618** |
|---|---|---|---|---|
| % soft tissue (based on x-value of trailing edge tip) | 43% | 26% | - | - |
| Chord length | ~ 0.39 m | ~ 0.24 m | - | - |
| Max camber (% chord length) | 11% | 11% | 6% | 3.3% |
| Location of max camber (% chord length) | 54% | 63% | 57% | 50% |
| Max thickness (% chord length) | 13% | 22% | 14% | 18% |
| Location of max thickness (% chord length) | 29% | 36% | 31% | 35% |
| Re | 390,000 | 240,000 | 390,000 | 240,000 |
| $C_{Lmax}$ | 1.95 | 2.02 | 1.82 | 1.44 |
| $C_{Dmin}$ | 0.013 | 0.042 | 0.009 | 0.013 |
| Max L / D | 78.0 | 16.5 | 115.8 | 79.8 |
| Stall angle | 20.5º | 26.75º | 19.75º | 20.5º |

Table 3: Inviscid comparison of lift coefficient ($C_L$) at $\alpha = 10º$ among the *C. eurymerus* hydrofoils, cetacean flukes from various taxa taken at rest (from Fish et al., 2007), and engineered airfoils with (NACA 63(3)-618 and Wortmann FX 63-137) and without camber (NACA 0021).

| **Species / Designation** | **Hydrofoil element cross-section** | **$C_L$** |
|---|---|---|
| *Cryptoclidus eurymerus* | Distal cross-section of humerus | 2.57 |
| *Cryptoclidus eurymerus* | Distal cross-section of femur | 2.77 |
| *Delphinus delphis* | Cross-section at 50% of fluke span | 1.16 |
| *Globicephala malaena* | Cross-section at 50% of fluke span | 1.27 |
| *Grampus griseus* | Cross-section at 50% of fluke span | 1.32 |
| *Kogia breviceps* | Cross-section at 50% of fluke span | 1.26 |
| *Lagenorhynchus acutus* | Cross-section at 50% of fluke span | 1.33 |
| *Phocoena phocoena* | Cross-section at 50% of fluke span | 1.29 |
| *Stenella* sp. | Cross-section at 50% of fluke span | 1.31 |
| *Tursiops truncatus* | Cross-section at 50% of fluke span | 1.34 |
| NACA 0021 | - | 1.29 |
| NACA 63(3)-618 | - | 1.82 |
| Wortmann FX 63-137 | - | 2.24 |

## DISCUSSION

The method described here is the first to quantitatively reconstruct the trailing edge soft tissue and resulting functional shape of the plesiosaur flipper (Figure 11, 13, and 16). This enables, for the first time, the quantification of the hydrodynamic properties of plesiosaur flippers. This method was applied to the distal cross-section of the *C. eurymerus* humerus and femur resulting in the reconstructions shown in Figure 11 for the femur and Figure 14 for the humerus. Now that the functional shape of the flipper is complete, the chord length, camber, and thickness distribution of the flipper could be obtained and used to assess the hydrodynamic properties, such as lift and drag, that emerge from the hydrofoil geometry (Table 2).

The hydrodynamic properties of the reconstructed humerus and femur hydrofoils were assessed using XFoil and a Re value calculated using equation 1 from the chord length of each hydrofoil respectively, a flow velocity of 1 m/s based on estimates of optimal swimming speed for *Cryptoclidus* by Motani (2002), and the kinematic viscosity of water (Table 2). At these respective Re values, the reconstructed hydrofoils for the humerus and femur have similar values of $C_{Lmax}$ (~ 2, see Table 2). However, the humerus hydrofoil has a lower value of $C_{Dmin}$ than the femur hydrofoil (0.013 compared to 0.042, respectively; Table 2) due in part to the lower thickness of the humerus. This results in a higher maximum L/D ratio for the humerus hydrofoil (78.0 compared to 16.5, respectively; Table 2). Interestingly, the reconstructed humerus and the femur hydrofoils have very similar maximum camber (11%, relative to chord length; Table 2). This relatively high camber endows the *C. eurymerus* hydrofoils with high $C_{Lmax}$ values and large stall angles (Table 2 and 3). The $C_{Lmax}$ values for the *C. eurymerus* hydrofoils are noticeably greater than those for cetacean fluke hydrofoils taken at rest, which has little to no camber (Table 3) (Fish et al., 2006; 2007). The NACA 0021 airfoil, which has zero camber,

produces a $C_{Lmax}$ value within the range of values for the cetacean fluke hydrofoils while the cambered Wortmann FX 63-137 and NACA 63(3)-618 airfoils fall in the same range of values as the *C. eurymerus* hydrofoils (Table 3). When compared side-by-side, the *C. eurymerus* humerus has modestly greater camber than the similarly shaped Wortmann FX 63-137 airfoil. Consequently, under the same Re value (390,000) the humerus hydrofoil and the Wortmann FX 63-137 airfoil have similar $C_{Lmax}$ values and stall angles (1.95 vs 1.82 and 20.5º vs 19.75º respectively; Table 2). The difference in camber is greater between the *C. eurymerus* femur hydrofoil and the similarly shaped NACA 63(3)-618 airfoil (11% vs 3% relative to chord length; Table 2). Consequently compared to the NACA 63(3)-618 airfoil, the femur hydrofoil has greater $C_{Lmax}$ (2.02 vs 1.44) and greater stall angle (26.75º vs 20.5º) under the same Re value (240,000; see Table 2). However, the maximum L/D ratio is greater for the Wortmann FX 63-137 and the NACA 63(3)-618 airfoil than for the *C. eurymerus* humerus and femur hydrofoils, respectively, due to the lower $C_{Dmin}$ values attained by the engineered airfoils.

*Cryptoclidus eurymerus* was a slow but maneuverable swimmer. The hydrodynamic properties of the reconstructed hydrofoils for the distal cross-section of the humerus and femur for *C. eurymerus* presented in this study suggest that the fore and hind flippers are adapted for slow swimming with high maneuverability. The most prominent feature of both hydrofoils is the high degree of camber, which results in high $C_{Lmax}$ values and high stall angles. This prevents the loss of lift (and hence thrust) at slow speeds resulting in greater maneuverability. The rearward position of maximum camber (past 50% of chord length; see Table 2) further aids maneuverability by reducing the drop in $C_L$ immediately following the stall angle (Abbott and von Doenhoff, 1959). The planform shape of the flippers (Figure 7) further supports a slow, but maneuverable specialization for the flippers. Reconstructed in Figure 15 is the planform shape

of the fore flipper and hind flipper incorporating the reconstructed hydrofoil cross-sections of the humerus and femur, respectively. The fore and hind flippers both have low aspect ratios (ARs), based on the skeletal elements of the flippers alone (O'Keefe, 2001b). When combined with the reconstructed trailing edges at the distal tip of the humerus and femur, the planform shape becomes even broader further reducing the AR (Figure 15). Low AR hydrofoils are not as efficient as those with high AR (ratio of $C_L/C_D$ is smaller) but, in exchange, enable slower speeds and higher maneuverability (Vogel, 1994), a trend observed in birds (O'Keefe, 2001b) and cetaceans (Woodward et al., 2006; Fish 2004). Part of the reduction in efficiency is the larger value of $C_D$ due to greater induced drag (Vogel, 1994). This is reduced by a distally tapering planform and by having a sweepback (Kucherman, 1953; Ashenberg and Weihs, 1984). These are both features of the fore and hind flippers of *C. eurymerus* (Figure 7, 15). Importantly, the degree of taper is pronounced in the fore flipper and the sweepback is strongly exaggerated (Figure 7, 15). The humerus extends anteriorly, unlike in any other plesiosaur, and from there, the rest of the flipper starting with the radius and ulna angles posteriorly (Figure 7, 15). Altogether, the *C. eurymerus* flippers enable slow swimming speeds and greater maneuverability based on a high $C_{Lmax}$ value, a high stall angle (Table 2), and a low AR planform coupled to a distally tapering planform with pronounced sweepback that reduces drag.

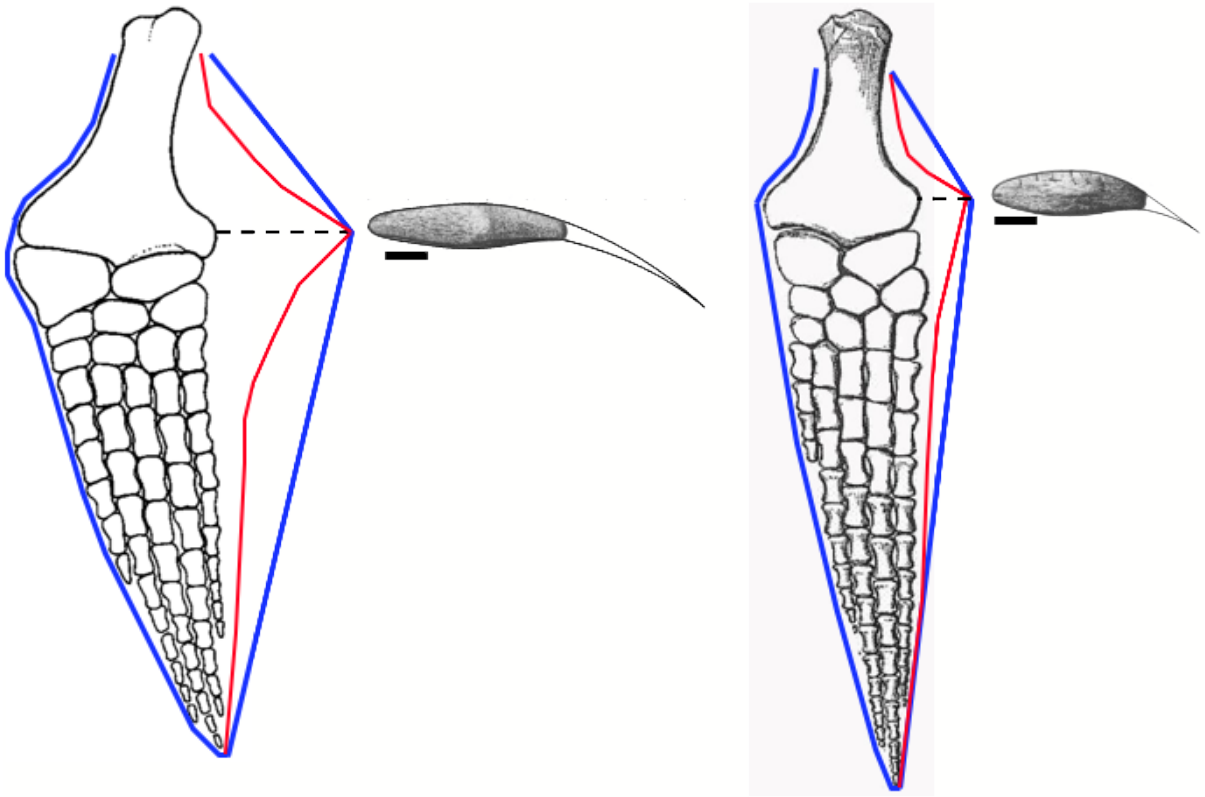

Figure 15. Planform reconstruction of the fore flipper and hind flipper of *Cryptoclidus eurymerus* (on the left and right, respectively). In blue is the outline of the planform made by connecting the tip of the reconstructed trailing edge at the distal end of the propodial to the tip of the phalanges. In red is the outline of another possible planform. The more cross-sectional hydrofoil shapes are reconstructed, the better the resolution of the shape of the flipper will be. The skeletal reconstruction of the flipper planform is from Storrs (1993) for the fore flipper and Andrews (1910) for the hind flipper. Scale bar = 5 cm.

Although the exact anatomy of the plesiosaur flipper is impossible to ascertain, the functional shape of the plesiosaur flipper is approximated using the quantitative method presented here with only a few assumptions and simplifications. The first assumption is that the shape of the fossil element closely matches the functional shape of the flipper with soft tissue intact. As Figure 6 illustrates in extant animals, the bones that make up the flipper (Figure 6c) is responsible for the cross-sectional hydrofoil shape. The soft tissue that surrounds the bone

follows its curvature such that the shape formed by the outline of the bones is reflected in the shape of the functional hydrofoil. Soft tissue increases the overall size of the hydrofoil but does not obscure the shape formed by the bones. Therefore, it is reasonable to use the outline of the fossil bones to derive the functional shape of the flipper.

Another assumption is that the best functioning hydrofoil (top 5% L/D) would also be a likely shape for the plesiosaur flipper hydrofoil. This assumption was used as the basis for constraining the set of possible hydrofoil shapes for the fossil element from the thousands tested by the method. Webber and colleagues (2009) compared idealized physical representations of several cetacean flipper hydrofoils and compared their hydrodynamic properties to real, anatomical flippers. They found the idealized flippers to underestimate the $C_D$ value of the real flipper they were supposed to mimic. Likewise, the true plesiosaur flipper was likely to be sub-optimal. However, identifying the degree to which the flipper of an extinct animal is sub-optimal is extremely difficult, if not impossible. Using best performance as criterion is more manageable and easier to apply and also sets the limit on what is possible.

Steady flow is also assumed. The performance of the hydrofoil shapes were analyzed and compared to one another under steady flow. In an actively swimming animal the direction and magnitude of flow around the flippers would change during the stroke cycle. However, whether or not the flow around the flipper could be accurately simplified as steady or unsteady could be calculated and is given by the aerodynamic frequency parameter (also known as the reduced frequency value), ω, which is a measure of the unsteady effects of flow about the hydrofoil:

$$\omega = 2\pi f c/U \tag{20}$$

where $f$ is the wingbeat frequency, $c$ is the chord of the hydrofoil (Figure 4), and $U$ is the velocity of the flow. For dolphins, $\omega > 0.5$ (Fish 1993), which suggests that the steady flow around the flippers cannot be assumed. The same is likely to be also true for plesiosaurs. However, the method does not aim to determine the kinematics of the plesiosaur flipper during the stroke cycle. Steady flow is used only to characterize the hydrodynamic properties of the shapes in order to identify the best functional hydrofoil shape for the fossil element.

The L/D ratio of the candidate hydrofoils for Re = 10,000,00 is used to determine the best performing hydrofoil shape. This relatively high Re value was chosen in order to bypass the transition from laminar to turbulent flow, which occurs between 500,000 and 1,000,000, and simplify the behavior of the flowstream. This is within the range of Re experienced by the body of swimming dolphins as a whole (Fish, 1993) and is likely within the range of Re experienced by the body of plesiosaurs as a whole as well (mentioned in Motani, 2002). However, the shorter length of the flipper cross-section compared to the whole animal would mean that the Re experienced by the hydrofoil would be smaller. That is, unless the velocity of the flipper motion makes up for the smaller length of the flipper during the stroke cycle by being proportionally higher than the velocity of the animal (see equation 1). However, consideration of the kinematics of the stroke cycle is beyond the scope of XFoil and, hence, the method used here. Since the length of the functional flipper changes with every hydrofoil shape candidate, the Re was kept constant and instead the speed of the flow about the hydrofoil was allowed to change (see equation 1). Alternatively, the speed could have been kept constant that the Re calculated for each hydrofoil shape. However, doing so would entail considerable additional programming

since the Re value would have to be calculated for each hydrofoil shape and its input into XFoil for each of the thousands of hydrofoil shapes would have to be automatized.

Lastly, the assumptions and simplifications inherent to using XFoil also apply to the present method. The values of $C_L$ and $C_D$ are obtained by calculating and applying potential flow over a mathematically determined boundary layer and laminar-to-turbulent transition. XFoil is sufficient to obtain a rough estimate of the hydrodynamic properties of the hydrofoil shapes in order to obtain the functionally best performing shape. Subsequent in-depth investigations and characterizations of the hydrofoil shape should be reserved for more sophisticated programs and, ideally, flow tank experiments using physical models.

The method introduced in this study is the first to quantitatively reconstruct the cross-sectional shape of the plesiosaur flipper hydrofoil. It was used to reconstruct the trailing edge soft and resulting hydrofoil shape of the distal propodial of the plesiosaur *C. eurymerus*. However, it could just as easily have been applied to any cross-section along the length of the flipper assuming the shape of the fossil elements is intact and separate elements properly articulated. Furthermore, this method is not limited to plesiosaur flippers but could also be applied to approximate the shapes and hydrodynamic properties of flippers from other extinct taxa like ichthyosaurs.

# CHAPTER 3: FUTURE WORK – VALIDATION EXPERIMENTS

## INTRODUCTION

A few assumptions and simplifications were made in the method introduced in this study in order to address the problem of reconstructing the soft tissue that forms the trailing edge of the plesiosaur flipper. One is that the best functional hydrofoil shape closely approximates the shape of the real plesiosaur hydrofoil. The other is that the best functional hydrofoil shape would be the same no matter the Reynolds number (Re) used. The first is addressed by taking a cross-section of a hydrofoil from an extant animal such as the fluke and flipper hydrofoils of whales and the wing of a penguin, removing some portion of the trailing edge, then comparing the best functional shape obtained with the method to the full cross-section of the flipper. The second is addressed by using different Re values to determine the best functional shape of the hydrofoil for the same fossil element, *e. g.* the *Cryptoclidus eurymerus* femur.

## METHOD

In Part 1, the same method introduced in Chapter 2 is used here to determine the functional shape of truncated whale fluke and penguin wing hydrofoils. In Part 2, the same method as in Chapter 2 will be used and once again applied to the *C. eurymerus* femur except the Re number will be varied.

## PRELIMINARY DATA

The contour plots for *C. eurymerus* femur corresponding to Re of $10^7$, $10^6$, 500,000 and 250,000 are shown in Figure 16.

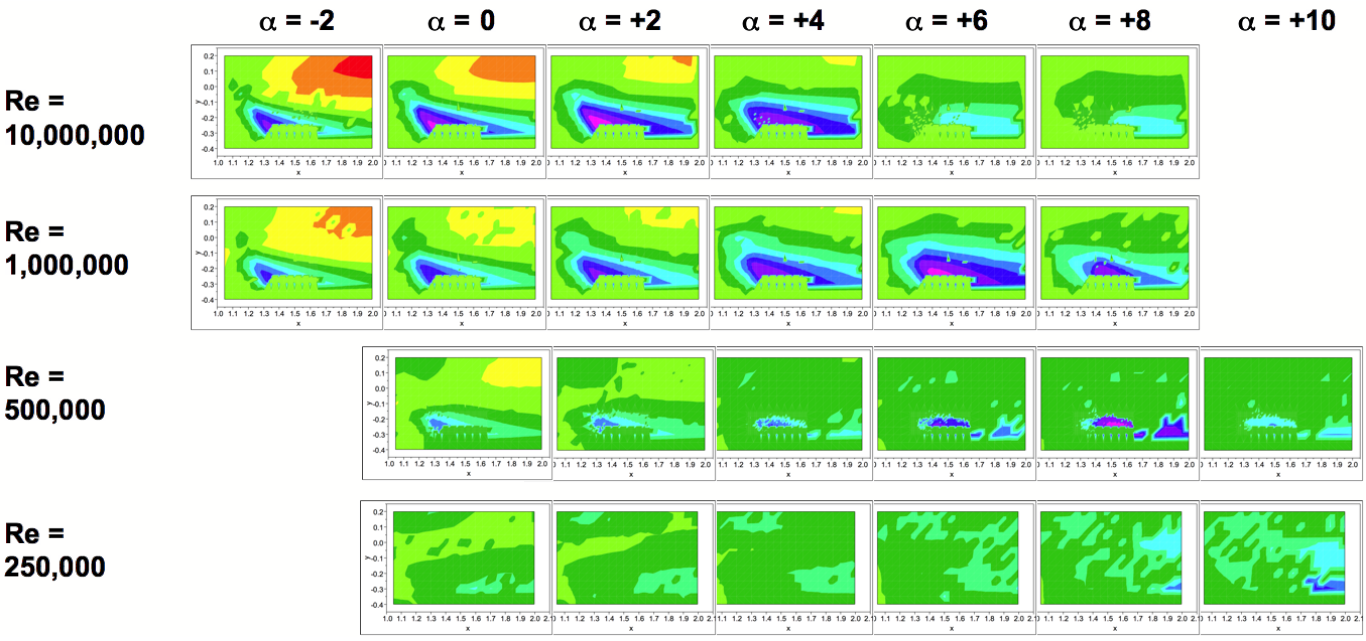


Figure 16. Contour plots for the *C. eurymerus* femur at Re = 10,000,000; Re = 1,000,000; Re = 500,000; and Re = 250,000 for α between -2º and +10º.

## INTERPRETATION

Reducing the Re increases the angle of attack (α) at which the highest L/D ratio occurs (Figure 16). The general topography stays the same however and no noticeable differences occur in the x,y-coordinate location of the trailing edge tip that produces a hydrofoil shape with the highest L/D ratio. An in-depth analysis should be performed in order to ascertain that changing Re has minimal effect on the shape of the best performing hydrofoil.

# CHAPTER 4: FUTURE WORK – PLESIOSAUR FLIPPER KINEMATIC HYPOTHESIS

## INTRODUCTION

A few assumptions and simplifications were made in the methods that preclude a kinematic analysis of the plesiosaur flipper, specifically the steady flow assumption. However, without losing sight of this caveat, it is possible to use the method presented here to develop a kinematic hypothesis for the plesiosaur stroke cycle. This hypothesis could then be tested more rigorously with the appropriate program simulator or flow tank experiments with physical models. The logic is that the most effective angles of attack ($\alpha$) would reflect changes in the direction of flow that occur during the stroke cycle. The best $\alpha$ could be interpreted as the dominant angle of attack and the lower and upper bounds of the most effective $\alpha$ could be interpreted as the limits of range of motion. Additionally, since the shape of plesiosaur flipper hydrofoil would be changing during the stroke cycle as $\alpha$ changes (Figure 17), one could then take the best performing shapes (highest L/D) for each $\alpha$ and reconstruct the shape changes that occur during the stroke cycle. I present one such hypothesis for the kinematics of the *Cryptoclidus eurymerus* hind flipper here, at the level of the femur.

## METHOD

From the set of candidate *C. eurymerus* femur hydrofoils obtained in the study in Chapter 2, a subset is created comprised of the best performing hydrofoil shape and the other hydrofoil shapes that have the same mean line length. The mean line follows the curvature of the hydrofoil and so would be a good indicator of flipper length. From this subset, the best performing shape

is determined for each $\alpha$. The shapes are then placed in order based on $\alpha$ to reconstruct the full range of changes that accompany the stroke cycle. Consideration is given to the $\alpha$ that produces the highest L/D as this likely dominates the stroke cycle.

## PRELIMINARY DATA

For the *C. eurymerus* femur, the best performing hydrofoil shape (assuming steady flow with no turbulence and a relatively high Reynolds number) is shown in Figure 11 and again in Figure 17. The trailing edge that corresponds to this shape is in black. The cyan-colored trailing edges are other trailing edge shapes that did not perform as well as the one in black but have the same length (measured via the mean of the top and bottom surface coordinates, within ±2.5% of the length of the best performing hydrofoil). Since the trailing edge is made up of soft tissue and likely to be flexible, these auxiliary shapes might be different forms of the same trailing edge.

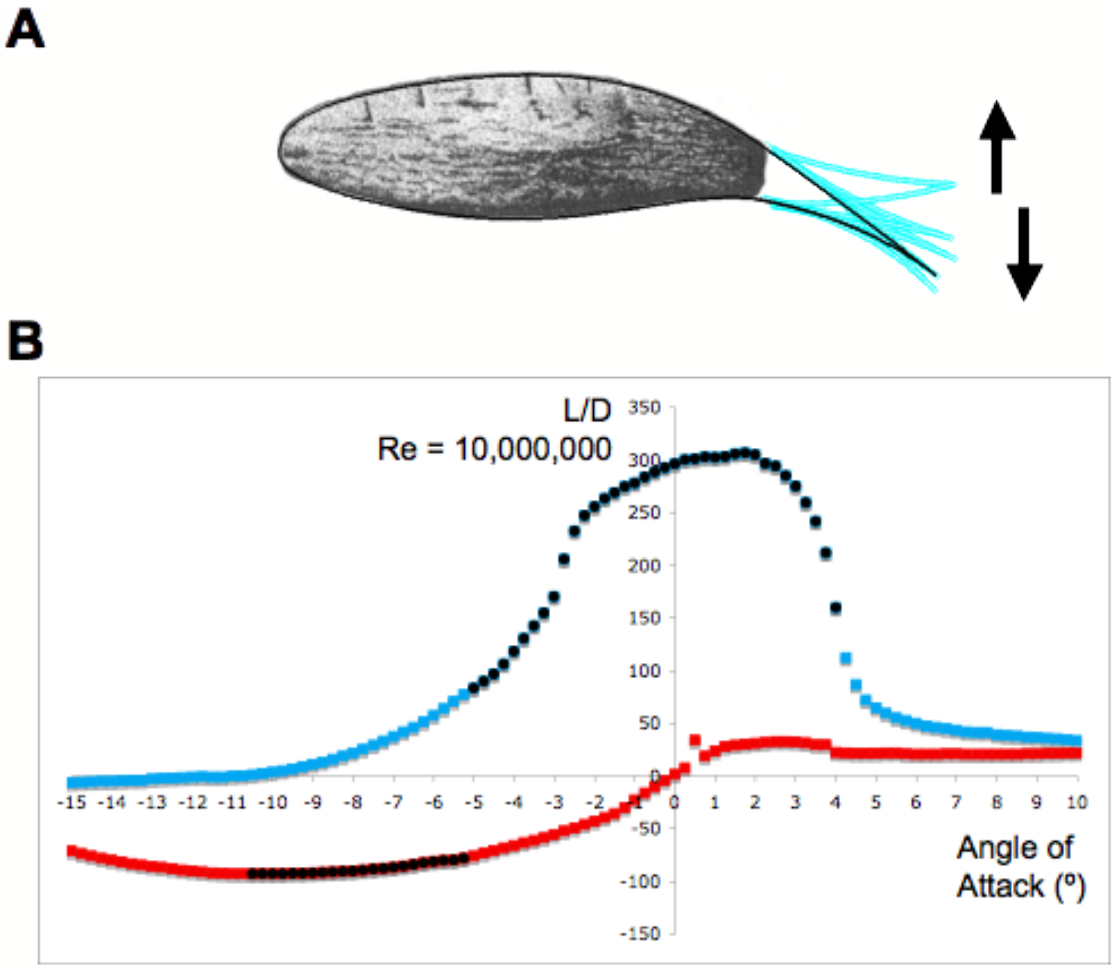


Figure 17. Shown in (**A**) is the best functional hydrofoil shape for the *Cryptoclidus eurymerus* femur (in black) superimposed on top of the other hydrofoil shapes that have the same mean line length (in cyan). These shapes are hypothesized to be the shapes the hydrofoil shapes that arise during the stroke cycle as the trailing edge soft tissue deflects/moves up and down. In (**B**) is plotted the highest L/D values at Re = 10,000,000 for the hydrofoil shapes that have the same mean line length as the best functional hydrofoil.

## INTERPRETATION

The changes in shape of the hydrofoil trailing edge at corresponding angles of attack reflect the kinematics of the femur stroke cycle. The femur is more effective at producing a dorsally oriented lift vector (Figure 17), which coincides with the asymmetric, dorsally oriented

camber of the fossil cross-section (not including the trailing edge). This means that for the power stroke the dorsal side of the flipper must have a forward directed component with respect to the animal. This is achieved parsimoniously in a forward-moving animal only if the dorsal side of the flipper is tilted forward in addition to a downward movement of the hydrofoil; only then will the net flow locally around the hydrofoil have a rearward and upward orientation that together with the forward tilt of the hydrofoil produces a forward directed lift component. Upward movement of the hydrofoil would orient the dorsal side of the hydrofoil backward and would lead to a rearward facing lift component. Therefore, the power stroke must be the downstroke. Furthermore, the most effective angle of attack (highest L/D magnitude) is around 0º, which coincides with a forward tilted hydrofoil facing a rearward and upward flow stream. This angle of attack and corresponding trailing edge shape likely dominates the downstroke. As the angle of attack increases to +4º (Figures 17) the orientation of the trailing edge switches from ventral to dorsal, which in turn changes the curvature of the hydrofoil from having dorsally oriented camber (convex side up) to having ventrally oriented camber (convex side down). The top and bottom flow streams separate beyond +4º, which suggests that the transition from positive to negative angles of attack occurs at +4º. This signals the transition from one stroke to the other, from downstroke to upstroke. The switch in sign of the L/D value at -5.25º marks the other stroke transition, from upstroke to downstroke. At the start of the upstroke, the angle of attack is shallower than at the downstroke, around -10º. A shift in angle of attack in the negative direction would result if the magnitude of the rearward flow stream is much larger than the downward flow stream (upward motion of the flipper). Since the hydrofoil now has a ventral camber (convex side down) and consequently the lift vector is oriented toward the ventral side of the hydrofoil, upward movement continues to produce a forward oriented lift component,

although not as much as in the downstroke. Towards the end of the upstroke, the angle of attack approaches -5º. At the end of the upstroke the trailing edge flips back to the ventral side (convex side up) and the hydrofoil tilts sharply to a downward orientation with an angle of attack of -5º. Altogether, the swimming motion of the femur is as follows: at the start of the downstroke, the hydrofoil is angled sharply downward with an angle of attack around -5º; the hydrofoil then tilts quickly to an angle of attack around 0º and maintains this angle for most of the downstroke; towards the bottom of the stroke, the hydrofoil tilts further up to an angle of attack at +4º at the bottom; at the same time, the trailing edge of the hydrofoil transitions from curving ventrally (convex side up) to curving dorsally (convex side down); this marks the end of the downstroke and the start of the upstroke; at this point the flipper is cambered ventrally (convex side down); the magnitude of the velocity of the upstroke is not as large as the downstroke, consequently the hydrofoil has a shallower upstroke angle of attack; towards the end of the upstroke, the angle of attack sharpens to -5º before reaching the end of the upstroke; at this point the hydrofoil trailing edge quickly switches back to its ventral oriented position (convex side up) and tilts to a downward angle of attack of -5º, at which point the cycle repeats.

# CHAPTER 5: FUTURE WORK – FUNCTIONAL EVOLUTION OF THE SHAPE AND HYDRODYNAMIC PROPERTIES OF THE PLESIOSAUR FLIPPER

## INTRODUCTION

This method enables a functional analysis of the evolution of flippers shapes across plesiosaur phylogeny as well as provides a way to constrain inference about plesiosaur paleoecology based on the hydrodynamic properties of the flippers. For instance, the hypothesized ecomorphology of the plesiosauromorph and pliosauromorph body plans could now be tested by quantitatively comparing the hydrodynamic properties of their respective flippers. If plesiosauromorphs are indeed cruising predators, then their flippers should favor high efficiency (high L/D) at the expense of maneuverability. Conversely, if pliosauromorphs are active-pursuit predators that have to chase down nimble prey, then their flippers should favor high maneuverability at the expense of efficiency.

## METHOD

The soft tissue and flipper hydrofoil reconstruction method will be applied to propodial cross-sections from a range of plesiosaur taxa in order to trace the geometric and functional changes that occurred in the evolution of crown-group taxa such as the pliosauromorph members of Pliosauridae and the plesiosauromorph members of Elasmosauridae.

## PRELIMINARY DATA

The best functional hydrofoil shapes were reconstructed for the plesiosaurs belonging to Rhomaleosauridae, Microcleididae (including *Westphaliasaurus*), Elasmosauridae, Cryptocleididae, and Polycotylidae (Table 4). The reconstructed flipper hydrofoils are shown in Figure 18 below. The same *Cryptoclidus eurymerus* humerus and flipper specimens (HMG V1104) from the study described in Chapter 2 are included in this study.

## INTERPRETATION

Pending hydrodynamic characterization of the hydrofoil shapes, interpretation is limited to discussion of overt differences in shape. The size of the reconstructed trailing edges are very long for some taxa especially *Microcleidus* (Figure 18). The orientation of camber also varies across taxa with a surprising predominance of ventral directed (convex side down) camber in the femur of the specimens sampled (Figure 18). Further analysis and inclusion of more taxa is needed in order to identify any trends.

Figure 18 (next page). The reconstructed hydrofoil shapes for the distal cross-sections of the propodial from various taxa within Plesiosauria. *Westphaliasaurus simonsensii* (humerus and femur, Westfälischen Museum für Naturkunde in Münster museum WMNM P58091) from Schwermann and Sander, 2011; *Callowayasaurus colombiensis* (University of California Museum of Paleontology, UCMP 38349); *Cryptoclidus eurymerus* (humerus and femur, The Hunterian Museum, Glasgow HMG V1104) from Brown, 1981.

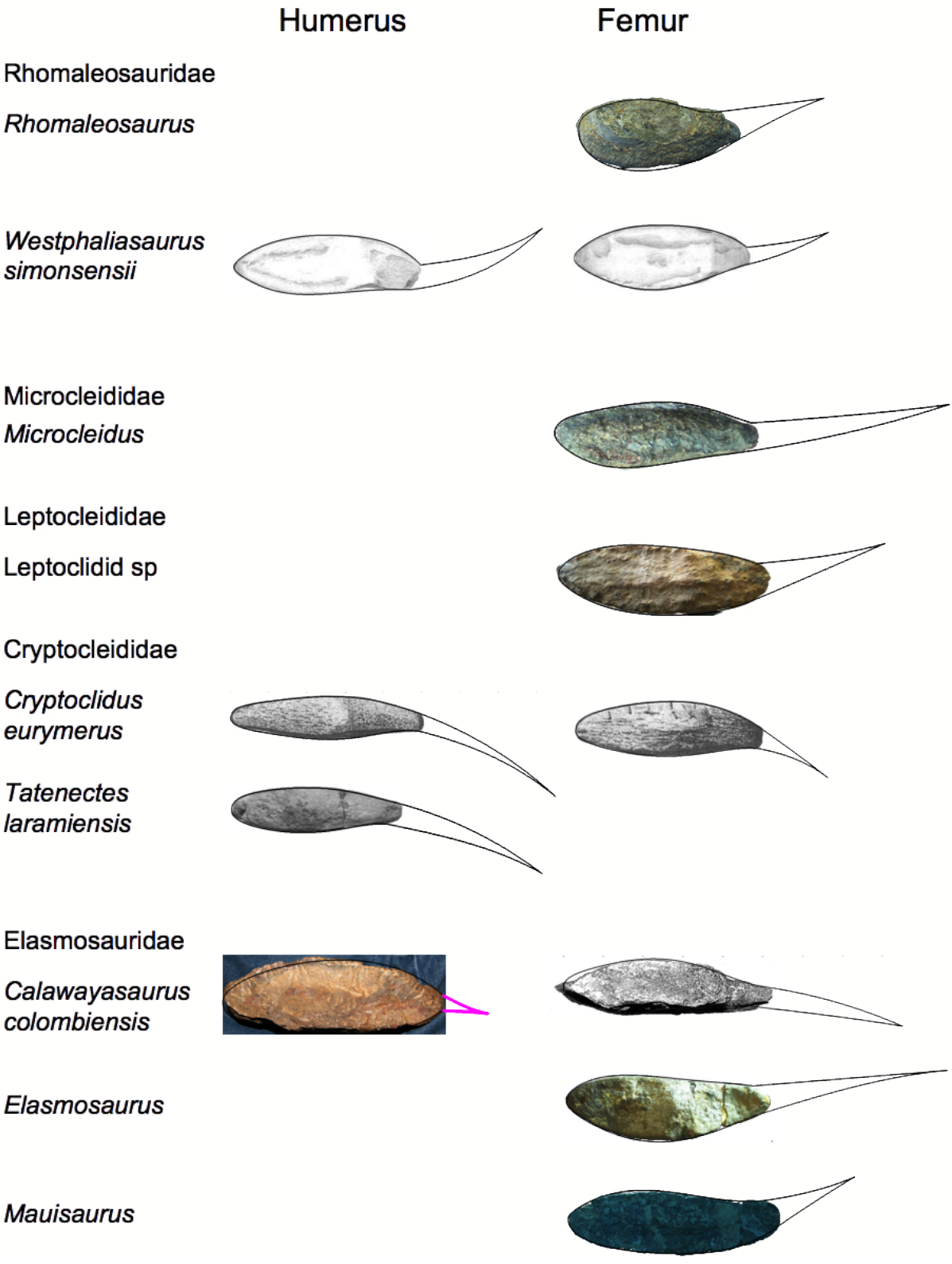
Humerus
Femur
Rhomaleosauridae
Rhomaleosaurus
Westphaliasaurus simonsensii
Microcleididae
Microcleidus
Leptocleididae
Leptoclidid sp
Cryptocleididae
Cryptoclidus eurymerus
Tatenectes laramiensis
Elasmosauridae
Calawayasaurus colombiensis
Elasmosaurus
Mauisaurus

# CHAPTER 6: FUTURE WORK – THREE-DIMENSIONAL MODELS

The method introduced in this study is the first to quantitatively address the problem of reconstructing the soft tissue that forms the trailing edge of the plesiosaur flipper. In order to do so, it was necessary to determine the L/D of the candidate hydrofoil shapes (reconstructed trailing edge + fossil outline). The airfoil design and simulation program XFoil was used for this purpose. However, even though viscous-inviscid formulation of XFoil takes into account boundary layers and flow transitions (laminar to turbulent), it still only calculates the potential flow. XFoil is a good program to use as a first estimate but more in-depth study of the hydrodynamics of the plesiosaur flipper would require a more sophisticated program (such as OpenFOAM) and, ideally, experiments using flow tanks and physical models. The best functional hydrofoil shape for the plesiosaur flipper cross-section could be determined out of the set of candidate hydrofoil shapes using a program like OpenFOAM. Then the two-dimensional hydrodynamic properties of this hydrofoil could be determined using flow tanks and a two-dimensional model. Furthermore, the dynamics of the soft tissue trailing edge could be studied in-depth with a model with a stiff body but flexible trailing edge tail. The experimental set-up could be designed as in (Prempraneerach and Triantafyllou, 2003).

Eventually the flipper hydrofoil cross-sections along the length of the flipper will be reconstructed, including at least one cross-section at the epipodial, mesopodial, metapodial, and phalanges (Figure 5). This way the hydrodynamic properties of the hydrofoils all along the length of the flipper could be analyzed and combined to investigate the hydrodynamics of the entire flipper. A three-dimensional model of the entire flipper would be tested using experiments using flow tanks.

# LITERATURE CITED

Abbott IH and von Doenhoff AE. 1959. *Theory of Wing Sections*. Dover, New York.

Althaus D and Wortmann FX. 1981. *Stuttgarter Profilkatalog I.* Friedr. Veiweg & Sohn. Braunshweig/Weisbaden.

Ashenberg J and Weihs D. 1984. Minimum induced drag of wings with curved planform. *J. Aircr*. 21: 89-91.

Andrews CW. 1910. *A descriptive catalogue of marine reptiles of the Oxford Clay Part 1*. British Museum (Natural History), London.

Andrews CW. 1913. *A descriptive catalogue of marine reptiles of the Oxford Clay Part 2*. British Museum (Natural History), London.

Bannasch, R. 1994. Functional anatomy of the 'flight' apparatus in penguins. In *Mechanics and Physiology of Animal Swimming* (eds Maddock L, Bone Q, and Rayner JMV), pp. 133-149. Cambridge University Press. New York, NY.

Benson RBJ, Evans M, and Druckenmiller PS. 2012. High diversity, low disparaty and small body size in plesiosaurs (Reptilia, Sauropterygia) from the Triassic – Jurassic boundary. *PLoS ONE* 7(3): e31838. doi:10.1371/journal.pone.0031838.

Brown DS. 1981. The English Upper Jurassic Plesiosauroidea (Reptilia) and a review of the phylogeny and classification of the Plesiosauria. *Bulletin of the British Museum (Natural History), Geology*. 35: 253-347.

Brown DS and Cruickshank ARI. 1994. The skull of the Callovian plesiosaur *Cryptoclidus eurymerus* and the sauropterygian cheek. *Palaeontology*. 37(4): 941-953.

Caroll RL. 1981. Plesiosaur ancestors from the Upper Permian of Madagascar. *Philosophical Transactions of the Royal Society of London, B*. 293(1066): pp. 315-383.

Carpenter K. 2007. Comparative cranial anatomy of two North American Cretaceous plesiosaurs. In *Ancient Marine Reptiles* (eds Calloway, JM and Nicholls E), pp. 191-216. Academic Press, San Diego.

Carpenter K, Sanders F, Reed B, Reed J, and Larson P. 2010. Plesiosaur swimming as interpreted from skeletal analysis and experimental results. *Transactions of the Kansas Academy of Science*. 113(1/2): 1-34.

Cooper LH, Dawson SD, Reindenberg JS, and Berta A. 2007. Neuromusctular anatomy and evolution of the cetacean forelimb. *The Anatomical Record*. 290:1121-1137.

Cooper LH, Sedano N, Johansson S, May B, Brown JD, Holliday CM, Kot BW, and Fish FE. 2008. Hydrodynamic performance of the minke whale (*Balaenoptera acutorostrata*) flipper. *The Journal of Experimental Biology*. 211: 1859-1867.

Cruickshank RI and Fordyce RE. 2002. A new marine reptile (Sauroptrygia) from New Zealand: further evidence for a late Cretaceous austral radiation of cryptoclidid plesiosaurs. *Palaeontology*. 45(3): 557-575.

Davenport J, Munks SA, and Oxford PJ. 1984. A comparison of the swimming of marine and freshwater turtles. *Proceedings of the Royal Society of London, B*. 220: 447-475.

De La Beche HT and Conybeare WD. 1821. Notice of the discovery of a new fossil animal, forming a link between the *Ichthyosaurus* and crocodile, together with general remarks on the osteology of the *Ichthyosaurus*. *Transactions of the Geological Society of London*. 5: 559-594.

Dodd, CK. 1988. Synopsis of the biological data on the Loggerhead Sea Turtle *Caretta caretta* (Linnaeus 1758). U.S. Fish Wildl. Serv., *Biol. Rep*. 88(14), pp. 110.

Drela M. 1989a. XFOIL: An analysis and design system for low Reynolds number airfoils. In *Low Reynolds Number Aerodynamics* (ed. Mueller TJ). Springer-Verlag Lecture Notes in Engineering #54. pp. 1-12. XFoil program last updated on November 30, 2001. http://web.mit.edu/drela/Public/web/xfoil/

Drela M. 1989b. Integral boundary layer formulation for blunt trailing edges. *AIAA Paper* 89-2200.

Drela M and Giles MB. 1987. Viscous-inviscid analysis of transonic and low Reynolds number airfoils. *AIAA Journal*. 25(10): 1347-1355.

Drela M and Youngren H. 2001. XFoil 6.94 User Guide. *Aerocraft, Inc*. pp 1-33.

Druckenmiller PS and Russel AP. 2008. A phylogeny of Plesiosauria (Sauropterygia) and its bearing on the systematic status of *Leptocleidus* Andrews, 1922. *Zootaxa*. 1863: 1-120.

Godfrey SJ. 1984. Plesiosaur subaqueous locomotion a reappraisal. *Neues Jahrbuch fur Geologie und Palaontologie, Monatshefte*. 11: 661-672.

Everhart MJ. 2000. Gastroliths associated with plesiosaur remains in the Sharon Springs member of the Pierre Shale (late Cretaceous), western Kansas. *Transactions of the Kansas Academy of Science*. 103(1-2):64-75.

Feldkamp SD. 2009. Foreflipper propulsion in the California sea lion, *Zalophus californicus*. *Journal of Zoology*. 212(1): 43-57.

Fearn R. 2008. Airfoil dynamics using panel methods. *Mathematica Journal*. 10(4): 726-739.

Fish FE. 1993. Power output and propulsive efficiency of swimming bottlenose dolphins (*Tursiops truncatus*). *Journal of Experimental Biology*. 185: 179-193.

Fish FE. 1998. Comparative kinematics and hydrodynamics of odontocete cetaceans: Morphological and ecological correlates with swimming performance. *Journal of Experimental Biology*. 201: 2867-2877.

Fish FE. 2004. Structure and mechanics of non-piscine control surfaces. *IEEE F. Oceanic Eng*. 29:605-621.

Fish FE, Beneski JT, and Ketten DR. 2007. Examination of the three-dimensional geometry of cetacean flukes using computed tomography scans: Hydrodynamic implications. *The Anatomical Record*. 290: 614-623.

Fish FE and Battle, JM. 1995. Hydrodynamic design of the humpback whale flipper. *Journal of Morphology*. 225:51-60.

Fish FE, Beneski JT, and Ketten DR. 2007. Examination of the three-dimensional geometry of cetacean flukes using computed tomography scans: Hydrodynamic implications. *The Anatomical Record*. 290: 614-623.

Fish FE, Nusbaum MK, Beneski JT and Ketten DR. 2006. Passive cambering and flexible propulsors: ceatacean flukes. *Bioinspiration & Biomimetics*. 1:S42-S48.

Fish FE, Innes S, and Ronald K. 1988. Kinematics and estimated thrust production of swimming harp and ringed seals. *Journal of Experimental Biology*. 137: 157-173.

Fontanella JE, Fish FE, Rybczynki N, Nweela MT, and Ketten DR. 2010. Three-dimensional geometry of the narwhal (*Monodon monoceros*) flukes in relation to hydrodynamics. *Marine Mammal Science*. 27(4): 889-898.

Frey E and Reiss J. 1982. Considerations concerning plesiosaur locomotion. *Neues Jahrbuch fur Geologie und Palaontologie, Abhandlungen*. 164(1-2):193-194.

Fritsch FN and Carlson RE. 1980. Monotone Piecewise Cubic Interpolation. *SIAM Journal of Numerical Analysis*, 17:238 – 246.

Habib, M. 2010. The structural mechanics and evolution of aquaflying birds. *Biological Journal of the Linnean Society*. 99:687-698.

Halstead LB. 1989. Plesiosaur locomotion. *Journal of the Geological Society, London*. 146: 37-40.

Henderson DM. 2006. Floating point: a computational study of buoyancy, equilibrium, and gastroliths in plesiosaurs. *Lethaia.* 39(3) pp. 227-244.

Ketchum HF and Bensom RBJ. 2010. Global interrelationships of Plesiosauria (Reptilia, Sauropterygia) and the pivotal role of taxon sampling in determining the outcome of phylogenetic analyses. *Biological Reviews* 85: 361-392.

Kear BP. 2003. Cretaceous marine reptiles of Australia: a review of taxonomy and distribution. *Cretaceous Research*. 24: 277-303.

Kear BP, Schroeder NI, Vickers-Rich P, and Rich TH. 2006. Early Cretaceous high latitude marine reptile assemblages from southern Australia. *Paludicola*. 5(4): 200-205.

Kuchermann D. 1953. The distribution of lift over the surface of swept wings. *Aeronaut. Quart.* 4: 261-278.

Kulfan BM and Bussoletti JE. 2006. "Fundamental" parametric geometry representations for aircraft component shapes. *American Institute of Aeronautics and Astronautics*. 1-45.

Lane KA and Marshall DD. 2009. A surface parametrization method for aircraft optimization and high lift 2D geometries utilizing the CST methodology. *American Institute of Aeronautics and Astronautics*. 1-13.

Lingham-Soliar, T. 2000. Plesiosaur locomotion: is the four-wing problem real or merely an atheoretical exercise? *Neues Jahrbuch fur Geologie und Palaontologie, Abhandlungen*. 217(1): 45-87.

Lovvorn JR. 2001. Upstroke thrust, drag effects, and stroke-glide cycles in wing-propelled swimming in birds. *American Zoologist*. 41:154-165.

Lovvorn JR and Liggins GA. 2002. Interactions of body shape, body size, and stroke-acceleration patterns in costs of underwater swimming by birds. *Functional Ecology.* 16:106-112.

Massare JA. 1988. Swimming capabilities of mesozoic marine reptiles: Implications for method of predation. *Paleobiology*. 14(2): 187-205.

Massare JA. 1994. Swimming capabilities of Mesozoic marine reptiles: a review. In *Mechanics and Physiology of Animal Swimming* (eds Maddock L, Bone Q, and Rayner JMV), pp. 133-149. Cambridge University Press. New York, NY.

Moler C. 2004. Numerical computing with MATLAB. *Society for Industrial and Applied Mathematics*.

Motani R. 2002. Swimming speed estimation of extinct marine reptiles: energetic approach revisited. *Paleobiology*. 28(2): 251 – 262.

Motani R. 2005. Ichthyosauria: evolution and physical constraints of fish-shaped reptiles. *Annual Review of Earth and Planetary Sciences*. 33:395-420.

Neenan JM, Klein N, and Scheyer TM. 2013. European origin of placodont marine reptiles and the evolution of crushing dentition in Placodontia. *Nature Communications*. 4(1621): 1-7.

Nicholls EL and Russell AP. 1990. Paleobiogeography of the Cretaceous Western Interior Seaway of North America: the vertebrate evidence. *Palaeogeography, Palaeoclimatology, Palaeoecology*. 79: 149-169.

O'Keefe FR. 2001a. A cladistic analysis and taxonomic revision of the Plesiosauria (Reptilia: Sauropterygia). *Acta Zoologica Fennica*. 213: 1-63.

O'Keefe FR. 2001b. Ecomorphology of plesiosaur flipper geometry. *J. Evol. Biol*. 14: 987-991.

O'Keefe FR. 2002. The evolution of plesiosaur and pliosaur morphotypes. *Paleobiology*. 28(1): 101-112.

O'Keefe FR and Carrano MT. 2005. Correlated trends in the evolution of the plesiosaur locomotor system. Paleobiology. 31(4): 656-675

Prempraneerach P, Hover FS, and Triantafyllou MS. 2003. The effect of chordwise flexibility on the thrust and efficiency of a flapping foil, in *13th Proc. Intern. Symp. Unmanned Untethered Submersible Technology*.

Rasband WS. 1997-2012. ImageJ. *U.S. National Institutes of Health*. Bethesda, MD, USA, http://imagej.nih.gov/ij/

Rieppel O. 1997. Introduction to Sauropterygia. In *Ancient Marine Reptiles* (eds Calloway, JM and Nicholls E), pp. 107-119. Academic Press, San Diego.

Rieppel O. 2000. Sauropterygia I. Placodontia, Pachypleurosauria, Nothosauroidea, Pistosauroidea. In Kuhn O and Wellnhofer P (eds.), *Encyclopedia of Paleoherpetology, Part 12A* 1-134. Verlag Dr. Friedrich Pfeil, Munchen, Germany.

Robinson JA. 1975. The locomotion of plesiosaurs. *Neues Jahrbuch fur Geologie und Palaontologie, Abhandlungen*. 149: 268-332.

Robinson JA. 1977. Intracorporal force transmission in plesiosaurs. *Neues Jahrbuch fur Geologie und Palaontologie, Abhandlungen*. 153, 86-128.

Sane SP. 2003. The aerodynamics of insect flight. *Journal of Experimental Biology*. 206: 4191-4208

Schwermann L and Sander PM. 2011. Osteologie und Phylogenie von Westphaliasaurus simonsensii: Ein neuer Plesiosauride (Sauropterygia) aus dem Unteren Jura (Pliensbachium) von Sommersell (Kreis Höxter), Nordrhein-Westfalen, Deutschland. *Geologie und Paläontologie in Westfalen* 79: 1-60

Selig MS and McGranahan BD. 2004. Wind tunnel aerodynamic tests of six airfoils for use on small wind turbines. *Journal of Solar Energy Engineering*. 126: 986-1001.

Smith AS. 2007. The back-to-front plesiosaur *Cryptoclidus (Apractocleidus) aldingeri* from the Kimmeridgian of Milne Land, Greenland. *Bulletin of the Geological Society of Denmark*. 55: 1-7.

Storrs GW. 1993. Function and phylogeny in sauropterygian (Diapsida) evolution. *American Journal of Science*. 293-A: 63-90.

Storrs GW. 1997. Morphological and taxonomic clarification of the genus *Plesiosaurus*. In *Ancient Marine Reptiles* (eds Calloway, JM and Nicholls E), pp. 145-190. Academic Press, San Diego.

Storrs GW. 1999. An examination of Plesiosauria (Diapsida: Sauropterygia) from the Niobara Chalk (Upper Cretaceous) of central North America. *The University of Kansas, Paleontological Contributions*. 11: 1-15.

Tarlo LB. 1957. The scapula of *Pliosaurus macromerus* Phillips. *Palaeontology* 1: 193-199.

Tarsitano S and Riess J. 1982. Plesiosaur locomotion – underwater flight versus rowing. *Neues Jahrburch fur Geologie und Plaontologie, Abhandlungen.* 164: 188-192.

Taylor MA. 1981. Plesiosaurs – rigging and ballasting. *Nature*. 290. 268-629.

Taylor MA. 1987. A reinterpretation of ichthyosaur swimming and buoyancy. *Paleontology*. 30(3): 531-535.

Taylor MA. 1993. Stomach stones for feeding or buoyancy? The occurrence and function of gastroliths in marine tetrapods. *Philosophical Transactions of the Royal Society of London B*. 341(1296): 163-175.

Thompson WA, Martin JE, and Reguero, M. 2007. Comparison of gastroliths within plesiosaurs (Elasmosauridae) from the Late Cretaceous marine deposits of Vega Island, Antarctic Peninsula, and the Missouri River area, South Dakota. *The Geological Society of America Special Paper* 427 pp. 147-153.

Vogel S. 1994. *Life in Moving Fluids*. Princeton University Press. Princeton, NJ.

von Huene F. 1923. Ein neuer Plesiosaurier aus dem oberen Lias Wurtembergs. *Jahreshefte des vereins fur Vaterlandische Naturkunde in Wurttemberg*. 79:1-21.

von Huene F. 1935. Ein plesiosaurier-rest aus Grönländischem Oberem Jura. *Kommissionen for Videnskabelige Under-søgelser I Grønland*. 99(4): 1-11.

Watson DMS. 1924. The elasmosaurid shoulder-girdle and fore-limb. *Proceedings of the*

*Zoological Society of London*. 28: 85-95.

Wahl WR, Massare JA, and Ross A. 2010. New material from the type specimen of *Megalneusaurus rex* (Reptilia: Sauropterygia) from the Jurassic Sundance Formation, Wyoming. *Paludicola.* 7(4): 170-180.

Webb PW. 1975. Hydrodynamics and energetics of fish propulsion. *Bull. Fish. Res. Bd. Can.* 190:1-159.

Webber PW, Murray MM, Howle LE and Fish FE. 2008. Comparison of real and idealized cetacean flippers. *Bioinspiration and Biomimetics*. 4: 1-12.

Welles SP. 1952. *A review of the North American Cretaceous elasmosaurs.* University of California Publication in Geological Sciences. 29:47-144.

Williston SW. 1903. *North American plesiosaurs*. Field Columbian Museum Publication. Chicago, IL. 11(1) pp. 156-157.

Williston SW. 1907. The skull of *Brachauchenius*, with observation of the relationships of the plesiosaurs. Proceedings of the National Museum 32 (Publication 1540): 477-493.

Woodward BL, Winn JP, and Fish, FE. 2006. Morphological specializations of baleen whales associated with hydrodynamic performance and ecological niche. *Journal of Morphology* 267:1284-1294.

Wynecken J. 1997. *Sea Turtle Locomotion: Mechanisms, Behavior, and Energetics*. In *The Biology of Sea Turtles* (eds Lutz PL and Musick JA), pp. 165-198. CRC Press, Boca Raton.

Wynecken J. 2001. The anatomy of sea turtles. *U.S. Department of Commerce NOAA Technical Memorandum NMFS-SEFSC-470*, pp. 1-172.

# APPENDIX

## QUANTITATIVE RECONSTRUCTION OF SOFT TISSUE CUSTOM MATLAB PROGRAM

```
% Plesiosaur Flipper Soft Tissue Quantitative Reconstructor
%
% Using Class - Shape Transformation (CST) Method by Kulfan and Bussoletti
% (2006)
%
%
% by Mark DeBlois
%
%
% Input arguments:
%   inputcurvetop  =  2-column matrix of x,y coordinates for the top curve.
%                     x-coordinates are raw x-values normalized to the
%                     largest raw x-value.
%                     Does not include the trailing edge tip coordinates,
%                     (xa,yb).
%   inputcurvebot  =  2-column matrix of x,y coordinates for the bottom
%                     curve.
%                     x-coordinates are raw x-values normalized to the
%                     largest raw x-value.
%                     Does not include trailing edge tip coordinates,
%                     (xa,yb).
%
%   alow      =  lower bound of x-coordinate values for test grid
%   ahigh     =  upper bound of x-coordinate values for test grid
%   amax      =  max number of x-coordinate points for test grid
%   blow      =  lower bound of y coordinate values for test grid
%   bhigh     =  upper bound of y coordinate values for test grid
%   bmax      =  max number of y-coordinate points for test grid
%             =  -blow + bhigh + 1 (1 is added to account for the set of
%                points where b = 0)



%x-coordinates of CST fitted curve of top and bottom outline after fitting
xnewtop = (0:0.001:1)';
xnewbot = (0:0.001:1)';

%Starting x- and y-coordinates
x0 = 1;
y0 = 0;

%x,y-coordinate interval (proportional to length of fossil element)
xinc = 0.01;
yinc = 0.01;
amax = (ahigh-alow)/xinc;
bmax = ((-blow/yinc)+(bhigh/yinc)+1);
xpchipwholetop = (0:0.0025:1)';
xpchipwholebot = (0:0.0025:1)';
count = 0;
%table of xa and yb coordinates
```

```
xycoordinates = zeros(amax*bmax+1,2);


%TOP CURVE
%Use CST Method to fit curve to raw outline

%Rotate so that endpoint is on x-axis
xrottop = inputcurvetop(:,1).*cos(atan(-inputcurvetop(1,2)/inputcurvetop...
    (1,1)))-inputcurvetop(:,2).*sin(atan(-inputcurvetop(1,2)/...
    inputcurvetop(1,1)));
yrottop = inputcurvetop(:,1).*sin(atan(-inputcurvetop(1,2)/inputcurvetop...
    (1,1)))+inputcurvetop(:,2).*cos(atan(-inputcurvetop(1,2)/...
    inputcurvetop(1,1)));

%Re-scale by max xrot value
xscaletop = xrottop./xrottop(1,1);
yscaletop = yrottop./xrottop(1,1);

%CST fit
Xtop0 = ones(1,4); %initial guess, all coefficients = 1
xtop = lsqnonlin(@fit_CSTtopBPO3,Xtop0,[],[],[],xscaletop,yscaletop);
ynewtop = CSTfittedtopBPO3(xtop,xnewtop);

%Undo scaling above to match native configuration of fossil outline
xrescaletop = xnewtop.*xrottop(1,1);
yrescaletop = ynewtop.*xrottop(1,1);

%Undo rotation above to match native configuration of fossil outline
xCSTtop = xrescaletop.*cos(atan(inputcurvetop(1,2)/inputcurvetop(1,1)))-...
    yrescaletop.*sin(atan(inputcurvetop(1,2)/inputcurvetop(1,1)));
yCSTtop = xrescaletop.*sin(atan(inputcurvetop(1,2)/inputcurvetop(1,1)))+...
    yrescaletop.*cos(atan(inputcurvetop(1,2)/inputcurvetop(1,1)));


%BOTTOM CURVE
%Use CST Method to fit curve to raw outline

%Rotate so that endpoint is on x-axis
xpchiprotbot = inputcurvebot(:,1).*cos(atan(-inputcurvebot(1,2)/...
    inputcurvebot(1,1)))-inputcurvebot(:,2).*sin(atan(-inputcurvebot...
    (1,2)/inputcurvebot(1,1)));
ypchiprotbot = inputcurvebot(:,1).*sin(atan(-inputcurvebot(1,2)/...
    inputcurvebot(1,1)))+inputcurvebot(:,2).*cos(atan(-inputcurvebot...
    (1,2)/inputcurvebot(1,1)));

%Re-scale by max xrot value
xscalebot = xpchiprotbot./xpchiprotbot(1,1);
yscalebot = ypchiprotbot./xpchiprotbot(1,1);

%CST fit
Xbot0 = ones(1,4); %initial guess, all coefficients = 1
xbot = lsqnonlin(@fit_CSTbotBPO3,Xbot0,[],[],[],xscalebot,yscalebot);
ynewbot = CSTfittedbotBPO3(xbot,xnewbot);

%Undo scaling above to match native configuration of fossil outline
xrescalebot = xnewbot.*xpchiprotbot(1,1);
```

```
yrescalebot = ynewbot.*xpchiprotbot(1,1);

%Undo rotation above to match native configuration of fossil outline
xCSTbot = xrescalebot.*cos(atan(inputcurvebot(1,2)/inputcurvebot(1,1)))-...
    yrescalebot.*sin(atan(inputcurvebot(1,2)/inputcurvebot(1,1)));
yCSTbot = xrescalebot.*sin(atan(inputcurvebot(1,2)/inputcurvebot(1,1)))+...
    yrescalebot.*cos(atan(inputcurvebot(1,2)/inputcurvebot(1,1)));


% Determine the first blow and bhigh x-value where the top and bottom
% curves do not cross, called the Lyndsay Boundary:  xlyndsaylow for blow,
% xlyndsayhigh for bhigh

xlyndsaymax = 10;
if amax > 10;
   xlyndsaymax = amax;
end
for a = (1:1:xlyndsaymax)
    xa = x0+a*(xinc);
    b = bhigh;
    yb = y0 + b;

    %Initial xlyndsay boundary
    xlyndsayhigh = 0;

    %TOP CURVE
    xfullsettop = [xa;xCSTtop];
    yfullsettop = [yb;yCSTtop];

    %Rotate bottom curve
    xpchiprottop = xfullsettop.*cos(atan(-yb/xa))-yfullsettop.*sin...
        (atan(-yb/xa));
    ypchiprottop = xfullsettop.*sin(atan(-yb/xa))+yfullsettop.*cos...
        (atan(-yb/xa));

    %Scale bottom curve
    xpchipscaletop = xpchiprottop./xpchiprottop(1,1);
    ypchipscaletop = ypchiprottop./xpchiprottop(1,1);

    %Interpolate to trailing edge tip coordinate (xa, yb)
    ypchipwholetop = interp1(xpchipscaletop,ypchipscaletop,...
        xpchipwholetop,'pchip');


    %BOTTOM CURVE
    xfullsetbot = [xCSTbot;xa];
    yfullsetbot = [yCSTbot;yb];

    %Rotate bottom curve
    xpchiprotbot = xfullsetbot.*cos(atan(-yb/xa))-yfullsetbot.*sin...
        (atan(-yb/xa));
    ypchiprotbot = xfullsetbot.*sin(atan(-yb/xa))+yfullsetbot.*cos...
        (atan(-yb/xa));

    %Scale bottom curve
    xpchipscalebot = xpchiprotbot./xpchiprotbot(end,1);
```

```
    ypchipscalebot = ypchiprotbot./xpchiprotbot(end,1);

    %Interpolate to trailing edge tip coordinate (xa, yb)
    ypchipwholebot = interp1(xpchipscalebot,ypchipscalebot,...
        xpchipwholebot,'pchip');

    if numel(ypchipwholebot(ypchipwholebot >= ypchipwholetop)) == 2;
       xlyndsayhigh = xa;
    break
    end
end

    if xlyndsayhigh == 0;
    disp...
 ('!! Trailing edge forms a loop for bhigh values at all values of xa. !!')
    break
    end

for a = (1:1:xlyndsaymax)
    xa = x0+a*(xinc);
    b = blow;
    yb = y0 + b;

    %Initial xlyndsay boundary
    xlyndsaylow = 0;

    %TOP CURVE
    xfullsettop = [xa;xCSTtop];
    yfullsettop = [yb;yCSTtop];

    %Rotate bottom curve
    xpchiprottop = xfullsettop.*cos(atan(-yb/xa))-yfullsettop.*sin...
        (atan(-yb/xa));
    ypchiprottop = xfullsettop.*sin(atan(-yb/xa))+yfullsettop.*cos...
        (atan(-yb/xa));

    %Scale bottom curve
    xpchipscaletop = xpchiprottop./xpchiprottop(1,1);
    ypchipscaletop = ypchiprottop./xpchiprottop(1,1);

    %Interpolate to trailing edge tip coordinate (xa, yb)
    ypchipwholetop = interp1(xpchipscaletop,ypchipscaletop,...
        xpchipwholetop,'pchip');


    %BOTTOM CURVE
    xfullsetbot = [xCSTbot;xa];
    yfullsetbot = [yCSTbot;yb];

    %Rotate bottom curve
    xpchiprotbot = xfullsetbot.*cos(atan(-yb/xa))-yfullsetbot.*sin...
        (atan(-yb/xa));
    ypchiprotbot = xfullsetbot.*sin(atan(-yb/xa))+yfullsetbot.*cos...
        (atan(-yb/xa));

    %Scale bottom curve
```

```
    xpchipscalebot = xpchiprotbot./xpchiprotbot(end,1);
    ypchipscalebot = ypchiprotbot./xpchiprotbot(end,1);

    %Interpolate to trailing edge tip coordinate (xa, yb)
    ypchipwholebot = interp1(xpchipscalebot,ypchipscalebot,...
        xpchipwholebot,'pchip');

    if numel(ypchipwholebot(ypchipwholebot >= ypchipwholetop)) == 2;
       xlyndsaylow = xa;
    break
    end
end

    if xlyndsaylow == 0;
    disp...
  ('!! Trailing edge forms a loop for blow values at all values of xa. !!')
    break
    end
%
if xlyndsayhigh >= xlyndsaylow;
    xlyndsay = xlyndsayhigh;
elseif xlyndsayhigh <= xlyndsaylow;
    xlyndsay = xlyndsaylow;
end
%
for a = (1:1:amax)
    xa = alow+a*(xinc);
    for b = (blow:yinc:bhigh)
        yb = y0 + b;


            %Use to fill in gaps when fine sampling
            %if rem(xa,5*xinc) == 0;
            %    continue
            %end

            %if rem(yb,5*yinc) == 0;
            %    continue
            %end

        %TOP CURVE
        xfullsettop = [xa;xCSTtop];
        yfullsettop = [yb;yCSTtop];

        %Rotate bottom curve so that endpoint is on x-axis
        xpchiprottop = xfullsettop.*cos(atan(-yb/xa))-yfullsettop.*sin...
            (atan(-yb/xa));
        ypchiprottop = xfullsettop.*sin(atan(-yb/xa))+yfullsettop.*cos...
            (atan(-yb/xa));

        %Scale bottom curve
        xpchipscaletop = xpchiprottop./xpchiprottop(1,1);
        ypchipscaletop = ypchiprottop./xpchiprottop(1,1);

        %Interpolate to trailing edge tip coordinate (xa, yb)
        ypchipwholetop = interp1(xpchipscaletop,ypchipscaletop,...
```

```
        xpchipwholetop,'pchip');


    %BOTTOM CURVE
    xfullsetbot = [xCSTbot;xa];
    yfullsetbot = [yCSTbot;yb];

    %Rotate bottom curve
    xpchiprotbot = xfullsetbot.*cos(atan(-yb/xa))-yfullsetbot.*sin(...
        atan(-yb/xa));
    ypchiprotbot = xfullsetbot.*sin(atan(-yb/xa))+yfullsetbot.*cos(...
        atan(-yb/xa));

    %Scale bottom curve
    xpchipscalebot = xpchiprotbot./xpchiprotbot(end,1);
    ypchipscalebot = ypchiprotbot./xpchiprotbot(end,1);
    %
    ypchipwholebot = interp1(xpchipscalebot,ypchipscalebot,...
        xpchipwholebot,'pchip');


    %Determine if the hydrofoil trailing edge forms a loop.


    if numel(ypchipwholebot(ypchipwholebot >= ...
            (ypchipwholetop-eps))) == 2;
        xpchipwhole = [flipud(xpchipwholetop);xpchipwholebot];
        ypchipwhole = [flipud(ypchipwholetop);ypchipwholebot];
        xnew = [xa;yb;xpchipwhole];
        ynew = [xa;yb;ypchipwhole];


%If hydrofoil trailing edge  loops, use the closest hydrofoilshape that
%does not loop and stretch this trailing edge to the endpoint being tested
%(xa,yb).

    elseif numel(ypchipwholebot(ypchipwholebot >= ...
            (ypchipwholetop-eps))) > 2;
            cmax = amax;
            if amax < 10;
                cmax = 10;
            end
        for c = 1:1:cmax;
            if xa > xlyndsay;
            xstretch = xa-c*xinc;
            elseif xa <= xlyndsay;
            xstretch = xa+c*xinc;
            end

        %TOP CURVE
        xfullsettop = [xstretch;xCSTtop];
        yfullsettop = [yb;yCSTtop];

        %Rotate top curve so that endpoint is on x-axis
        xpchiprottop = xfullsettop.*cos(atan(-yb/xstretch))-...
            yfullsettop.*sin(atan(-yb/xstretch));
```

```
ypchiprottop = xfullsettop.*sin(atan(-yb/xstretch))+...
    yfullsettop.*cos(atan(-yb/xstretch));

%Scale top curve
xpchipscaletop = xpchiprottop./xpchiprottop(1,1);
ypchipscaletop = ypchiprottop./xpchiprottop(1,1);

%Interpolate to trailing edge tip coordinate (xa, yb)
ypchipwholetop = interp1(xpchipscaletop,ypchipscaletop,...
    xpchipwholetop,'pchip');


%BOTTOM CURVE
xfullsetbot = [xCSTbot;xstretch];
yfullsetbot = [yCSTbot;yb];

%Rotate bottom curve so that endpoint is on x-axis
xpchiprotbot = xfullsetbot.*cos(atan(-yb/xstretch))-...
    yfullsetbot.*sin(atan(-yb/xstretch));
ypchiprotbot = xfullsetbot.*sin(atan(-yb/xstretch))+...
    yfullsetbot.*cos(atan(-yb/xstretch));

%Scale bottom curve
xpchipscalebot = xpchiprotbot./xpchiprotbot(end,1);
ypchipscalebot = ypchiprotbot./xpchiprotbot(end,1);

%Interpolate to trailing edge tip coordinate (xa, yb)
ypchipwholebot = interp1(xpchipscalebot,ypchipscalebot,...
    xpchipwholebot,'pchip');


%If the trailing edge interpolation still loops:
    if numel(ypchipwholebot(ypchipwholebot >= ...
            (ypchipwholetop-eps))) == 2;
    break
    elseif numel(ypchipwholebot(ypchipwholebot >= ...
            (ypchipwholetop-eps))) > 2;
        while xstretch == xlyndsay;

           %Redefine xlyndsay to be the lower xlyndsay boundary
            if xlyndsayhigh >= xlyndsaylow;
               xlyndsay = xlyndsaylow;
            elseif xlyndsayhigh <= xlyndsaylow;
               xlyndsay = xlyndsayhigh;
            elseif xlyndsay <= 1;
                break
            end
            for d = 1:1:cmax;
                xstretch = xa-d*xinc;


                %TOP CURVE
                xfullsettop = [xstretch;xCSTtop];
                yfullsettop = [yb;yCSTtop];

                %Rotate top curve so that endpoint is on x-axis
```

```
                xpchiprottop = xfullsettop.*cos(atan(-yb/...
                    xstretch))-yfullsettop.*sin(atan(-yb/...
                    xstretch));
                ypchiprottop = xfullsettop.*sin(atan(-yb/...
                    xstretch))+yfullsettop.*cos(atan(-yb/...
                    xstretch));

                %Scale top curve
                xpchipscaletop = xpchiprottop./...
                    xpchiprottop(1,1);
                ypchipscaletop = ypchiprottop./...
                    xpchiprottop(1,1);

            %Interpolate to trailing edge tip coordinate (xa, yb)
                ypchipwholetop = interp1(xpchipscaletop,...
                    ypchipscaletop,xpchipwholetop,'pchip');


                %BOTTOM CURVE
                xfullsetbot = [xCSTbot;xstretch];
                yfullsetbot = [yCSTbot;yb];

              %Rotate bottom curve so that endpoint is on x-axis
                xpchiprotbot = xfullsetbot.*cos(atan(-yb/...
                    xstretch))-yfullsetbot.*sin(atan(-yb/...
                    xstretch));
                ypchiprotbot = xfullsetbot.*sin(atan(-yb/...
                    xstretch))+yfullsetbot.*cos(atan(-yb/...
                    xstretch));

                %Scale bottom curve
                xpchipscalebot = xpchiprotbot./xpchiprotbot...
                    (end,1);
                ypchipscalebot = ypchiprotbot./xpchiprotbot...
                    (end,1);

            %Interpolate to trailing edge tip coordinate (xa, yb)
                ypchipwholebot = interp1(xpchipscalebot,...
                    ypchipscalebot,xpchipwholebot,'pchip');

                if numel(ypchipwholebot(ypchipwholebot >= ...
                        ypchipwholetop)) == 2;
                break
                end
              end
          end
      end
end

%Stretch the trailing edge

%TOP CURVE
%Undo scaling
xpchipnewtop = xpchipwholetop.*xpchiprottop(1,1);
ypchipnewtop = ypchipwholetop.*xpchiprottop(1,1);
```

```
%Undo rotation
xpchipnoscaletop0 = xpchipnewtop.*cos(atan(yb/xstretch))-...
    ypchipnewtop.*sin(atan(yb/xstretch));
ypchipnoscaletop0 = xpchipnewtop.*sin(atan(yb/xstretch))+...
    ypchipnewtop.*cos(atan(yb/xstretch));


%BOTTOM CURVE
%Undo scaling
xpchipnewbot = xpchipwholebot.*xpchiprotbot(end,1);
ypchipnewbot = ypchipwholebot.*xpchiprotbot(end,1);

%Undo rotation
xpchipnoscalebot0 = xpchipnewbot.*cos(atan(yb/xstretch))-...
    ypchipnewbot.*sin(atan(yb/xstretch));
ypchipnoscalebot0 = xpchipnewbot.*sin(atan(yb/xstretch))+...
    ypchipnewbot.*cos(atan(yb/xstretch));

%Stretch
%TOP CURVE
xstretchcurvetop = xpchipnoscaletop0(xpchipnoscaletop0>...
    xCSTtop(end,1));
ystretchcurvetop = ypchipnoscaletop0(xpchipnoscaletop0>...
    xCSTtop(end,1));

%BOTTOM CURVE
xstretchcurvebot = xpchipnoscalebot0(xpchipnoscalebot0>...
    xCSTbot(end,1));
ystretchcurvebot = ypchipnoscalebot0(xpchipnoscalebot0>...
    xCSTbot(end,1));

%Translate x
    if xstretchcurvetop(1,1) > xstretchcurvebot(1,1);
        xtranslate = xstretchcurvetop(1,1);
    else xtranslate = xstretchcurvebot(1,1);
    end

%TOP CURVE
xstretchcurvetop1 = xstretchcurvetop-xtranslate;

%Stretch tail x
xstretchtailtop1 = ((xa-xtranslate)/(xstretch-xtranslate)).*...
    xstretchcurvetop1;

%Undo translate x
xstretchtailtop = xstretchtailtop1+xtranslate;
ystretchtailtop = ystretchcurvetop(xstretchtailtop>=xtranslate);
xstretchtailtop = xstretchtailtop(xstretchtailtop>=xtranslate);
%

%
%BOTTOM CURVE
xstretchcurvebot1 = xstretchcurvebot-xtranslate;

%Stretch tail x
xstretchtailbot1 = ((xa-xtranslate)/(xstretch-xtranslate)).*...
```

```
    xstretchcurvebot1;

 %Undo translate x
xstretchtailbot = xstretchtailbot1+xtranslate;
ystretchtailbot = ystretchcurvebot(xstretchtailbot>=xtranslate);
xstretchtailbot = xstretchtailbot(xstretchtailbot>=xtranslate);


 %Chop initial PCHIP interpolated tail

 %TOP
 xpchipnoscaletop = xpchipnoscaletop0(xpchipnoscaletop0<=...
     xCSTtop(end,1));
 ypchipnoscaletop = ypchipnoscaletop0(xpchipnoscaletop0<=...
     xCSTtop(end,1));


 %BOTTOM
 xpchipnoscalebot = xpchipnoscalebot0(xpchipnoscalebot0<=...
     xCSTbot(end,1));
 ypchipnoscalebot = ypchipnoscalebot0(xpchipnoscalebot0<=...
     xCSTbot(end,1));



 %Recombine with stretched tail

 %TOP
 xstretchcurvefulltop = [xpchipnoscaletop;xstretchtailtop];
 ystretchcurvefulltop = [ypchipnoscaletop;ystretchtailtop];

 %BOTTOM
 xstretchcurvefullbot = [xpchipnoscalebot;xstretchtailbot];
 ystretchcurvefullbot = [ypchipnoscalebot;ystretchtailbot];

 %rotate TOP
 xstretchcurverottop = xstretchcurvefulltop.*cos...
     (atan(-yb/xa))-ystretchcurvefulltop.*sin(atan(-yb/xa));
 ystretchcurverottop = xstretchcurvefulltop.*sin...
     (atan(-yb/xa))+ystretchcurvefulltop.*cos(atan(-yb/xa));

 %rotate BOTTOM
 xstretchcurverotbot = xstretchcurvefullbot.*cos...
     (atan(-yb/xa))-ystretchcurvefullbot.*sin(atan(-yb/xa));
 ystretchcurverotbot = xstretchcurvefullbot.*sin...
     (atan(-yb/xa))+ystretchcurvefullbot.*cos(atan(-yb/xa));


 %scale by max x-value

 %TOP
 xstretchcurvescaletop = xstretchcurverottop./...
     xstretchcurverottop(end,1);
 ystretchcurvescaletop = ystretchcurverottop./...
     xstretchcurverottop(end,1);
```

```
            %BOTTOM
            xstretchcurvescalebot = xstretchcurverotbot./...
                xstretchcurverotbot(end,1);
            ystretchcurvescalebot = ystretchcurverotbot./...
                xstretchcurverotbot(end,1);


            %Fill-in gaps by interpolating again

            %TOP CURVE
            xstretchwholetop = xpchipwholetop;
            ystretchwholetop = interp1(xstretchcurvescaletop,...
                ystretchcurvescaletop,xpchipwholetop,'phip');

            %BOTTOM CURVE
            xstretchwholebot = xpchipwholebot;
            ystretchwholebot = interp1(xstretchcurvescalebot,...
                ystretchcurvescalebot,xpchipwholebot,'pchip');

            xstretchwhole = [flipud(xstretchwholetop);xstretchwholebot];
            ystretchwhole = [flipud(ystretchwholetop);ystretchwholebot];

            %Coordinates of reconstructed hydrofoil
            xnew = [xa;yb;xstretchwhole];
            ynew = [xa;yb;ystretchwhole];
            %
        end

        %Creat filename
        k = yb;
        i = xa;
        filename = sprintf('CeH%1.2f%+1.2f.dat',i,k);
        dlmwrite(filename,[xnew(3:end,1),ynew(3:end,1)]);

        %Continue to next trailing edge tip coordinate
        count = count+1;
        xycoordinates(count+1,:) = [xa,yb];
    end
end
```

```
function diff = fit_CSTtopBPO3(xtop,xscaletop,yscaletop)
%CST function using Bernstein Polynomial order (BPO) = 3

A=xtop(1);
B=xtop(2);
C=xtop(3);
D=xtop(4);
diff = (xscaletop.^0.5.*(1-xscaletop).*(A.*(1-xscaletop).^3+...
    B.*3.*(1-xscaletop).^2.*xscaletop+C.*3.*(1-xscaletop).*xscaletop.^2+...
    D.*xscaletop.^3))-yscaletop;

end
```

```
function fittedfunction = CSTfittedbotBPO3(xbot,xnewbot)
% New fitted y-coordinates for Bernstein Polynomial order (BPO) = 3

fittedfunction = xnewbot.^0.5.*(1-xnewbot).*(xbot(1).*(1-xnewbot).^3+...
    xbot(2).*3.*(1-xnewbot).^2.*xnewbot+...
    xbot(3).*3.*(1-xnewbot).*xnewbot.^2+xbot(4).*xnewbot.^3);
```

MARSHALL UNIVERSITY.
www.marshall.edu

Office of Research Integrity

April 2, 2013

Mark DeBlois
1665 6th Avenue Apt 23
Huntington, WV 25703

Dear Mr. DeBlois:

This letter is in response to the submitted thesis abstract titled "Plesiosaur Flipper Hydrodynamics". After assessing the abstract it has been deemed not to be human subject research and therefore exempt from oversight of the Marshall University Institutional Review Board (IRB). The Code of Federal Regulations (45CFR46) has set forth the criteria utilized in making this determination. Since the information in this study does not involve human subjects as defined in the above referenced instruction it is not considered human subject research. If there are any changes to the abstract you provided then you would need to resubmit that information to the Office of Research Integrity for review and a determination.

I appreciate your willingness to submit the abstract for determination. Please feel free to contact the Office of Research Integrity if you have any questions regarding future protocols that may require IRB review.

Sincerely,

Bruce F. Day, ThD, CIP
Director
Office of Research Integrity